Comparison of a Finite Difference and a Mixed Finite Element Formulation of the Uniaxial Perfectly Matched Layer

V. A. Bokil[a] and M. W. Buksas[b]

Center for Research in Scientific Computation[a]
North Carolina State University
Raleigh, NC 27695-8205
vabokil@ncsu.edu

CCS-4, Mail Stop D409[b]
Los Alamos National Laboratory
Los Alamos, NM 87544
mwbuksas@lanl.gov

April 14, 2006

Abstract: We consider the anisotropic uniaxial formulation of the perfectly matched layer model (UPML). We prove the decay of different energies for the UPML, under certain assumptions, to demonstrate the well-posedness of this formulation. We present and analyze a mixed finite element method for the time domain discretization of the UPML to simulate wave propagation in unbounded domains in two dimensions. On rectangles the spatial discretization uses bilinear finite elements for the electric field and the lowest order Raviart-Thomas divergence conforming elements for the magnetic field. We use a centered finite difference method for the time discretization. We compare the finite element technique presented to the finite difference time domain method (FDTD) via a stability, dispersion, phase error and numerical reflection coefficient analysis. We derive the reflection coefficient for the case of a semi-infinite layer to show consistency between the numerical and continuous models, and in the case of a finite PML to study the effects of terminating the absorbing layer. Finally, we demonstrate the effectiveness of the mixed finite element scheme by numerical examples and provide comparisons with the split field PML discretized by the FDTD method. In conclusion, we observe that the mixed finite element scheme for the PML model has absorbing properties that are comparable to the FDTD method.

Keywords: Perfectly matched layers, Mixed finite element methods, FDTD, Maxwell's equations.

Report Documentation Page

Form Approved
OMB No. 0704-0188

1. REPORT DATE	2. REPORT TYPE	3. DATES COVERED
14 APR 2006		**00-00-2006 to 00-00-2006**

4. TITLE AND SUBTITLE	5a. CONTRACT NUMBER
Comparison of a Finite Difference and a Mixed Finite Element Formulation of the Uniaxial Perfectly Matched Layer	5b. GRANT NUMBER
	5c. PROGRAM ELEMENT NUMBER
6. AUTHOR(S)	5d. PROJECT NUMBER
	5e. TASK NUMBER
	5f. WORK UNIT NUMBER
7. PERFORMING ORGANIZATION NAME(S) AND ADDRESS(ES) **Center for Research in Scientific Computation,North Carolina State University,Raleigh,NC,27695-8205**	8. PERFORMING ORGANIZATION REPORT NUMBER
9. SPONSORING/MONITORING AGENCY NAME(S) AND ADDRESS(ES)	10. SPONSOR/MONITOR'S ACRONYM(S)
	11. SPONSOR/MONITOR'S REPORT NUMBER(S)

12. DISTRIBUTION/AVAILABILITY STATEMENT
Approved for public release; distribution unlimited

13. SUPPLEMENTARY NOTES

14. ABSTRACT

15. SUBJECT TERMS

16. SECURITY CLASSIFICATION OF:			17. LIMITATION OF ABSTRACT	18. NUMBER OF PAGES	19a. NAME OF RESPONSIBLE PERSON
a. REPORT **unclassified**	b. ABSTRACT **unclassified**	c. THIS PAGE **unclassified**		**44**	

1 Introduction

The effective modeling of waves on unbounded domains by numerical methods, such as the finite difference method or the finite element method, is dependent on the particular absorbing boundary condition used to truncate the computational domain. In 1994, J. P. Berenger created the *perfectly matched layer* (PML) technique for the reflectionless absorption of electromagnetic waves in the time domain [6]. The PML is an absorbing layer that is placed around the computational domain of interest in order to attenuate outgoing radiation. Berenger showed that his PML model allowed perfect transmission of electromagnetic waves across the interface of the computational domain regardless of the frequency, polarization or angle of incidence of the waves. The waves are then attenuated exponentially with depth in the absorbing layers. Since its original inception in 1994 PML's have also extended their applicability in areas other than computational electromagnetics such as acoustics, elasticity, etc. [2, 3, 17, 18, 19].

The properties of the continuous PML model have been studied extensively and are well documented. The original *split field* PML proposed by Berenger involved a nonphysical splitting of Maxwell's equations resulting in non-Maxwellian fields and a weakly hyperbolic system [1]. A complex change of variables approach was used in [11, 30] to derive an equivalent PML model that did not require a splitting of Maxwell's equations. In [32], the authors observed that a material can possess reflectionless properties if it is assumed to be anisotropic. A single layer in this technique was termed *uniaxial* and the PML was referred to as the uniaxial PML (UPML). In this method modifications to Maxwell's equations are also not required and one obtains a strongly hyperbolic system. In [16, 26] further study of the anisotropic PML is carried out. Unlike Berenger's split field PML, which is a nonphysical medium, the anisotropic PML can be a physically realizable medium [30]. Thus, there are several reasons for using the anisotropic PML in numerical simulations. In [38] the authors show that the anisotropic PML and Berenger's split field PML produce the same tangential fields, however, the normal fields are different as the two methods satisfy different divergence conditions.

The finite depth of the absorbing layer allows the transmitted part of the wave to return to the computational domain. In addition, the discretization of Maxwell's equations introduces errors which cause the PML to be less than perfectly matched. Even so, it has been found that the PML medium can result in reflection errors as minute as -80 dB to -100 dB [6, 7, 11, 16]. There are a number of publications that study the properties of the finite difference time

domain (FDTD) method (Yee scheme [41]), applied to the PML model (e.g., see [33]). There are many open questions related to the numerical approximations to the PML equations. For example, there are empirical results related to the selection of the PML conductivities, but no rigorous proofs on the optimal values of these parameters which govern the numerical reflections produced due to discretization. In [14, 40, 28, 20] the authors study numerical errors in the discretized PML and consider various methods for the selection of optimal values of the PML conductivities.

There are significantly less publications that study the properties of the finite element method for the approximation of the PML equations. A comparison of the anisotropic PML to the split field PML of Berenger was performed in [38], in which the authors implement the anisotropic PML into an edge based finite element method for a second order formulation of Maxwell's equations. In [39] the authors use the lowest order as well as first order tangential vector finite element methods for the discretization of the electric field. They compare the performance of these elements with the FDTD method when a PML is used to terminate the computational domain. They show that the lowest order elements do not perform as well as the FDTD method, however, the first order elements can produce more accurate results than FDTD. The lowest order edge element is, however, a most commonly used finite element approximation in the literature and most of these implementations are in the frequency domain (for e.g., see [25, 34, 22]). A time domain mixed finite element method has been used in [13] along with mass lumping techniques to solve scattering problems on domains where a PML method based on the Zhao-Cangellaris's model is used to terminate the mesh [42]. The underlying partial differential equations in the Zhao-Cangellaris's PML model are second order in time, whereas the anisotropic uniaxial model consists of a system of first order PDE's.

In this paper, we present a mixed finite element method (FEM) for the discretization of the anisotropic uniaxial formulation of the UPML, by Sacks *et al.,* [32] in the time domain to simulate wave propagation on unbounded regions. We divide the computational domain into rectangles. On each rectangle, we use continuous piecewise bilinear finite elements to discretize the electric field and the Raviart-Thomas elements [31] to discretize the magnetic field. The degrees of freedom are staggered in space as in the FDTD scheme. We use a centered difference scheme in time again staggering the temporal components of the electric and magnetic fields. We study the numerical properties of the presented method and the effectiveness of the PML technique as an absorbing boundary condition for FEM. We provide comparisons of the numerical approximations of the PML model by the mixed FEM with

those by the FDTD method. The presented finite element method can be viewed as an averaged FDTD scheme on regular grids. We have used this method in problems of scattering type in [9]. A mixed finite element method was used for the discretization of a similar UPML formulation for the wave equation written as a system of first order PDE's in [8].

An advantage of the FEM is that it can model arbitrary complex geometrical structures effectively. We compare the UPML discretized by the finite element method with the split field PML of Berenger discretized by the FDTD method. These comparisons demonstrate that the PML technique is an effective absorbing boundary condition for the mixed finite element method which has comparable (with FDTD) absorbing properties. This implies that using mass lumping techniques [5] one can use the PML method as a good absorbing boundary condition with FEM for problems involving complicated geometrical structures. The mass lumping techniques can help in significantly lowering costs associated with the implementation of the finite element method and, thus, make it a more general alternative to the FDTD method for discretizing PML models.

In Sections 2 and 3, we describe the UPML model and its implementation. In Section 4, we derive the two-dimensional (2D) transverse magnetic (TM) mode of the UPML model, and we describe a mixed finite element formulation for the UPML. We state some energy decay results that indicate the well-posedness of the PML model in Section 5. Section 6 describes the numerical discretization in space and time. We perform a dispersion and stability analysis in Section 7.1, a phase error analysis in Section 7.2 and a reflection coefficient analysis in Section 7.3. In both these analyses, we provide comparison of the properties of the mixed finite element method with the FDTD method. Finally, we present numerical examples in Section 8 that demonstrate the effectiveness of the discrete PML model for FEM. We also compare these numerical results with those of the split field method of Berenger discretized by the FDTD method.

2 An Anisotropic Perfectly Matched Layer Model

We begin with a form of Maxwell's equations, suitable for general media, which permits both electric and magnetic currents but does not contain unbalanced electric charges

$$\begin{aligned}
&\frac{\partial \mathbf{B}}{\partial t} = -\nabla\times\mathbf{E} - \mathbf{J_M}, \text{ (Maxwell-Faraday's Law)},\\
&\frac{\partial \mathbf{D}}{\partial t} = \nabla\times\mathbf{H} - \mathbf{J_E}, \text{ (Maxwell-Ampere's Law)},\\
&\nabla\cdot\mathbf{B} = 0, \text{ (Gauss's Law for the magnetic field)},\\
&\nabla\cdot\mathbf{D} = 0, \text{ (Gauss's Law for the electric field)}.
\end{aligned} \tag{2.1}$$

Constitutive relations which relate the electric and magnetic fluxes $(\mathbf{D}, \mathbf{B})$ and the electric and magnetic currents $(\mathbf{J_E}, \mathbf{J_M})$ to the electric and magnetic fields $(\mathbf{E}, \mathbf{H})$ are added to these equations to make the system fully determined and to describe the response of a material to the electromagnetic fields. In free space, these constitutive relations are $\mathbf{D} = \epsilon_0\mathbf{E}$ and $\mathbf{B} = \mu_0\mathbf{H}$, and $\mathbf{J_E} = \mathbf{J_M} = 0$, where ϵ_0, and μ_0 are the permittivity, and the permeability of free space, respectively. In general, there are different possible forms for these constitutive relationships. In a frequency domain formulation of Maxwell's equations, these can be converted to linear relationships between the dependent and independent quantities with frequency dependent coefficient parameters.

We will derive a PML model in the frequency domain and then obtain a PML model in the time domain by taking the inverse Fourier transforms of the frequency domain equations. To this end, we consider the time-harmonic form of Maxwell's equations (2.1) (with time dependence $e^{\mathrm{i}\omega t}$) given by

$$\begin{aligned}
&\mathrm{i}\omega\hat{\mathbf{B}} = -\nabla\times\hat{\mathbf{E}} - \hat{\mathbf{J}}_M,\\
&\mathrm{i}\omega\hat{\mathbf{D}} = \nabla\times\hat{\mathbf{H}} - \hat{\mathbf{J}}_E,\\
&\nabla\cdot\hat{\mathbf{B}} = 0,\\
&\nabla\cdot\hat{\mathbf{D}} = 0,
\end{aligned} \tag{2.2}$$

where for every field vector $\mathbf{V}$, $\hat{\mathbf{V}}$ denotes its Fourier transform and we have the constitutive laws

$$\hat{\mathbf{B}} = [\mu]\hat{\mathbf{H}}, \quad \hat{\mathbf{D}} = [\epsilon]\hat{\mathbf{E}}, \quad \hat{\mathbf{J}}_M = [\sigma_M]\hat{\mathbf{H}}, \quad \hat{\mathbf{J}}_E = [\sigma_E]\hat{\mathbf{E}}. \tag{2.3}$$

Here, the square brackets indicate a tensor quantity. Note that when the density of electric and magnetic charge carriers in the medium is uniform throughout space, then $\nabla \cdot \hat{\mathbf{J}}_E = 0$ and $\nabla \cdot \hat{\mathbf{J}}_M = 0$. We define new tensors

$$[\bar{\mu}] = [\mu] + \frac{[\sigma_M]}{\mathrm{i}\omega}; \quad [\bar{\epsilon}] = [\epsilon] + \frac{[\sigma_E]}{\mathrm{i}\omega}. \tag{2.4}$$

Using the definitions (2.4) we define two new constitutive laws that are equivalent to (2.3), given by

$$\hat{\mathbf{B}}_{\text{new}} = [\bar{\mu}]\hat{\mathbf{H}}; \quad \hat{\mathbf{D}}_{\text{new}} = [\bar{\epsilon}]\hat{\mathbf{E}}. \tag{2.5}$$

Using (2.5) in (2.2) Maxwell's equations in time-harmonic form become

$$\begin{aligned} \mathrm{i}\omega\hat{\mathbf{B}}_{\text{new}} &= -\nabla\times\hat{\mathbf{E}}, \\ \mathrm{i}\omega\hat{\mathbf{D}}_{\text{new}} &= \nabla\times\hat{\mathbf{H}}, \\ \nabla \cdot \hat{\mathbf{B}}_{\text{new}} &= 0, \\ \nabla \cdot \hat{\mathbf{D}}_{\text{new}} &= 0. \end{aligned} \tag{2.6}$$

The split-field PML introduced by Berenger [6] is a hypothetical medium based on a mathematical model. In [26] Mittra and Pekel showed that Berenger's PML was equivalent to Maxwell's equations with a diagonally anisotropic tensor appearing in the constitutive relations for $\mathbf{D}$ and $\mathbf{B}$. For a single interface the anisotropic medium is *uniaxial* and is composed of both the electric permittivity and magnetic permeability tensors. This uniaxial formulation performs as well as the original split-field PML while avoiding the nonphysical field splitting. As will be shown below, by properly defining a general constitutive tensor $[S]$, we can use the UPML in the interior working volume as well as the absorbing layer. This tensor provides a lossless isotropic medium in the primary computation zone, and individual UPML absorbers adjacent to the outer lattice boundary planes for mitigation of spurious wave reflections. The fields excited within the UPML are also plane wave in nature and satisfy Maxwell's curl equations.

The derivation of the PML properties for the tensor constitutive laws is also done directly by Sacks *et al.,* in [32] and by Gedney in [16]. We follow the derivation by Sacks *et al.,* here. We begin by considering planar electromagnetic waves in free space incident upon a PML half space. Starting with the impedance matching assumption, i.e., the impedance of the layer must match that of free space: $\epsilon_0^{-1}\mu_0 = [\bar{\epsilon}]^{-1}[\bar{\mu}]$ we have

$$\frac{[\bar{\epsilon}]}{\epsilon_0} = \frac{[\bar{\mu}]}{\mu_0} = [S] = \mathrm{diag}\{a_1, a_1, a_3\}. \tag{2.7}$$

Hence, the constitutive parameters inside the PML layer are $[\bar{\epsilon}] = \epsilon_0[S]$, and $[\bar{\mu}] = \mu_0[S]$, where $[S]$ is a diagonal tensor.

We consider plane wave solutions of the form $\mathbf{V}(\mathbf{x},t) = \hat{\mathbf{V}}(\mathbf{x})\mathrm{e}^{\mathrm{i}(\omega t - \mathbf{k}\cdot\mathbf{x})}$, for all field vectors $\mathbf{V}$, to the time-harmonic Maxwell's equations with the diagonally anisotropic tensor $[S]$. Here $\mathbf{k} = (k_x, k_y, k_z)$ is the wave vector of the planar electromagnetic wave and $\mathbf{x} = (x, y, z)$. In this case, the dispersion relation for waves in the PML are found to be

$$\frac{k_x^2}{a_2 a_3} + \frac{k_y^2}{a_1 a_3} + \frac{k_z^2}{a_1 a_2} = k_0^2 \equiv \omega^2 \mu_0 \epsilon_0 \equiv \frac{\omega^2}{c^2}, \tag{2.8}$$

where c is the speed of light in free space.

Without loss of generality we consider a PML layer which fills the positive x half-space and plane waves with wave vectors in the xy- plane ($k_z = 0$). Let θ_i be the angle of incidence of the plane wave measured from the normal to the surface $x = 0$. The standard phase and magnitude matching arguments at the interface yield a generalization of Snell's law

$$\sqrt{a_1 a_3}\sin\theta_t = \sin\theta_i, \tag{2.9}$$

where θ_t is the angle of the transmitted plane wave. By matching the magnitudes of the electric and magnetic fields at the interface, $x = 0$, the reflection coefficients for the transverse electric (TE) and the TM modes are given to be

$$R^{TE} = \frac{\cos\theta_i - \sqrt{\dfrac{a_3}{a_2}}\cos\theta_t}{\cos\theta_i + \sqrt{\dfrac{a_3}{a_2}}\cos\theta_t}; \quad R^{TM} = \frac{\sqrt{\dfrac{a_3}{a_2}}\cos\theta_t - \cos\theta_i}{\cos\theta_i + \sqrt{\dfrac{a_3}{a_2}}\cos\theta_t}. \tag{2.10}$$

From (2.10) we see that by choosing $a_3 = a_2 = a$ and $\sqrt{a_1 a_3} = 1$, the interface is completely reflectionless for any frequency and angle of incidence and polarization. Using (2.5) and (2.7) the constitutive laws for the perfectly matched layer are

$$\hat{\mathbf{B}}_{\text{new}} = \mu_0[S]\hat{\mathbf{H}}; \quad \hat{\mathbf{D}}_{\text{new}} = \epsilon_0[S]\hat{\mathbf{E}}, \tag{2.11}$$

where the tensor $[S]$ is given as

$$[S] = \begin{bmatrix} a^{-1} & 0 & 0 \\ 0 & a & 0 \\ 0 & 0 & a \end{bmatrix}. \tag{2.12}$$

The perfectly matched layer is therefore characterized by the single complex number a in the definition of the tensor $[S]$. Taking it to be the constant $a = \gamma - \mathrm{i}\beta$, and substituting

into the dispersion relation (2.8), we can obtain the expression

$$\hat{\mathbf{E}}(x,y,z) = \hat{\mathbf{E}}_0 \mathrm{e}^{-k_0\beta\cos\theta_t x} e^{-\mathrm{i}k_0(\gamma\cos\theta_t x + \sin\theta_t y)} e^{\mathrm{i}\omega t}, \tag{2.13}$$

for the electric field inside of the PML. Hence, we can see that γ determines the wavelength of the wave in the PML, and for $\beta > 0$ the wave is attenuated according to the distance of travel in the x direction.

3 Implementation of the Uniaxial PML

To apply the perfectly matched layer to electromagnetic computations the half infinite layer is replaced with a layer of finite depth and backed with a more conventional boundary condition, such as a perfect electric conductor (PEC). This truncation of the layer will lead to reflections generated at the PEC surface, which can propagate back through the layer to re-enter the computational region. In this case, the reflection coefficient R is a function of the angle of incidence θ, the depth of the PML δ, as well as the parameter a in (2.12). Thus, the parameter a for the PML is chosen in order for the attenuation of waves in the PML to be sufficient so that the waves striking the PEC surface are negligible in magnitude. Perfectly matched layers are then placed near each edge (face in 3D) of the computational domain where a non-reflecting condition is desired. This leads to overlapping PML regions in the corners of the domain. As shown in [32], the correct form of the tensor which appears in the constitutive laws for these regions is the product

$$[S] = [S]_x [S]_y [S]_z, \tag{3.1}$$

where component $[S]_\alpha$ in the product in (3.1) is responsible for attenuation in the α direction, for $\alpha = x, y, z$; see Figure 1. All three of the component tensors in (3.1) are diagonal and have the forms

$$[S]_x = \begin{bmatrix} s_x^{-1} & 0 & 0 \\ 0 & s_x & 0 \\ 0 & 0 & s_x \end{bmatrix}; \quad [S]_y = \begin{bmatrix} s_y & 0 & 0 \\ 0 & s_y^{-1} & 0 \\ 0 & 0 & s_y \end{bmatrix}; \quad [S]_z = \begin{bmatrix} s_z & 0 & 0 \\ 0 & s_z & 0 \\ 0 & 0 & s_z^{-1} \end{bmatrix}. \tag{3.2}$$

In the above s_x, s_y, s_z are analogous to the complex valued parameter a encountered in Section 2, in the analysis of a single PML layer. Here s_α governs the attenuation of the electromagnetic waves in the α direction for $\alpha = x, y, z$.

When designing PML's for implementation it is important to choose the parameters s_α so that the resulting frequency domain equations can be easily converted back into the time

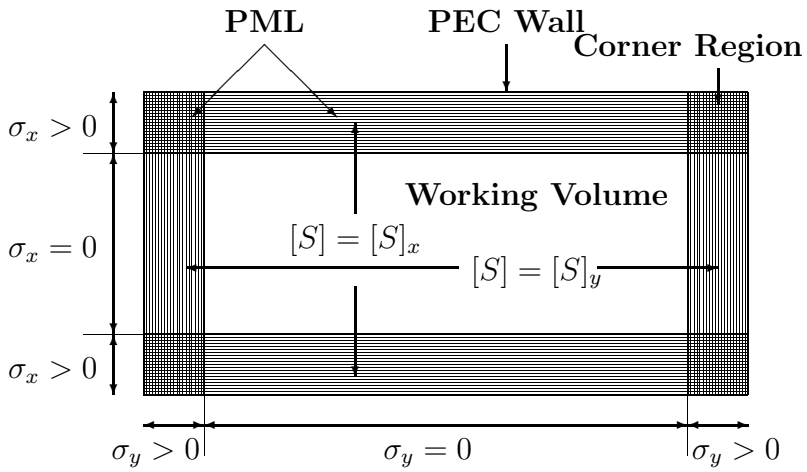

Figure 1: PML layers surrounding the domain of interest. The PML conductivities σ_x and σ_y are both zero in the working volume. The PML is truncated by a perfect electric conductor.

domain. The simplest of these which we employ here [16] is

$$s_\alpha = 1 + \frac{\sigma_\alpha}{\mathrm{i}\omega\epsilon_0}, \quad \text{where} \quad \sigma_\alpha \geq 0, \quad \alpha = x, y, z. \tag{3.3}$$

The PML interface represents a discontinuity in the conductivities σ_α. To reduce the numerical reflections caused by these discontinuous conductivities the σ_α are chosen to be functions of the variable α (for e.g., σ_x is taken to be a function of x in the $[S]_x$ component of the PML tensor). Choosing these functions so that $\sigma_\alpha = 0$, i.e., $s_\alpha = 1$ at the interface makes the PML a continuous extension of the medium being matched and reduces numerical reflections at the interface. Increasing the value of σ_α with depth in the layer allows for greater overall attenuation while keeping down the numerical reflections. Gedney [16] suggests a conductivity profile

$$\sigma_\alpha(\alpha) = \frac{\sigma_{\max}|\alpha - \alpha_0|^m}{\delta^m}, \quad \alpha = x, y, z, \tag{3.4}$$

where δ is the depth of the layer, $\alpha = \alpha_0$ is the interface between the PML and the computational domain, and m is the order of the polynomial variation. Gedney remarks that values of m between 3 and 4 are believed to be optimal. For the conductivity profile (3.4) the PML parameters can be determined for given values of m, δ, and the desired reflection

coefficient at normal incidence R_0 as

$$\sigma_{\max} \approx \frac{(m+1)\ln(1/R_0)}{2Z\delta}, \tag{3.5}$$

Z being the characteristic wave impedance of the PML. Empirical testing suggests [16] that, for a broad range of problems, an optimal value of $\sigma_{\max}$ is given by

$$\sigma_{\text{opt}} \approx \frac{m+1}{150\pi h_\alpha \sqrt{\epsilon_r}}, \tag{3.6}$$

where h_α is the space increment in the α direction and ϵ_r is the relative permittivity of the material being modeled. In the case of free space the relative permittivity is $\epsilon_r = 1$.

4 A Mixed Finite Element Formulation for the UPML in Two Dimensions

From the time-harmonic Maxwell's curl equations in the UPML (2.6) and (2.11), Ampere's and Faraday's laws can be written in the most general form as

$$\begin{cases} \mathrm{i}\omega\mu_0[S]\hat{\mathbf{H}} &= -\nabla\times\hat{\mathbf{E}} \quad ; \quad \text{(Maxwell-Faraday's Law)}, \\ \mathrm{i}\omega\epsilon_0[S]\hat{\mathbf{E}} &= \nabla\times\hat{\mathbf{H}} \quad ; \quad \text{(Maxwell-Ampere's Law)}. \end{cases} \tag{4.1}$$

In (4.1), $[S]$ is the diagonal tensor defined via (3.1)-(3.5). In the presence of this diagonal tensor, a plane wave is purely transmitted into the uniaxial medium. The tensor $[S]$ is no longer uniaxial by strict definition but rather is anisotropic. However, the anisotropic PML is still referenced as uniaxial since it is uniaxial in the non overlapping PML regions.

To obtain the 2D model of the UPML we assume no variation in the z direction (i.e., $\partial z = 0$). In the 2D TM mode the electromagnetic field has three components E_z, H_x, and H_y. Let $\partial_q = \partial q$ denote the derivative w.r.t q, for $q = x, y, z, t$. In this case, we have $\sigma_z = 0$ and $s_z = 1$ in the UPML, and the time-harmonic Maxwell's equations (4.1) in the uniaxial medium can be written in scalar form as

$$\begin{cases} \mathrm{i}\omega\mu_0 \dfrac{s_y}{s_x}\hat{H}_x &= -\partial_y\hat{E}_z, \\ \mathrm{i}\omega\mu_0 \dfrac{s_x}{s_y}\hat{H}_y &= -\partial_x\hat{E}_z, \\ \mathrm{i}\omega\epsilon_0 s_x s_y \hat{E}_z &= \partial_x\hat{H}_y - \partial_y\hat{H}_x. \end{cases} \tag{4.2}$$

To avoid a computationally intensive implementation we do not insert the expressions for s_x, s_y and s_z obtained via (3.3) into (4.2) and transform to the time domain. Instead we define

suitable constitutive relationships that facilitate the decoupling of the frequency dependent terms [33]. To this end, we introduce the fields

$$\left\{\begin{array}{rcl} \hat{B}_x &=& \mu_0 s_x^{-1}\hat{H}_x, \\ \hat{B}_y &=& \mu_0 s_y^{-1}\hat{H}_y, \\ \hat{D}_z &=& \mu_0 s_y \hat{E}_z. \end{array}\right. \tag{4.3}$$

Substituting the definitions (4.3) in (4.2), using the defining relations for s_x and s_y from (3.3), and then transforming into the time domain by using the inverse Fourier transform yields an equivalent system of time-domain differential equations given as

$$\left\{\begin{array}{lll} \text{(i)} & \partial_t B_x &= -\dfrac{\sigma_y}{\epsilon_0}B_x - \partial_y E_z, \\ \text{(ii)} & \partial_t H_x &= \dfrac{1}{\mu_0}\partial_t B_x + \dfrac{\sigma_x}{\epsilon_0\mu_0}B_x, \\ \text{(iii)} & \partial_t B_y &= -\dfrac{\sigma_x}{\epsilon_0}B_y + \partial_x E_z, \\ \text{(iv)} & \partial_t H_y &= \dfrac{1}{\mu_0}\partial_t B_y + \dfrac{\sigma_y}{\epsilon_0\mu_0}B_y, \\ \text{(v)} & \partial_t D_z &= -\dfrac{\sigma_x}{\epsilon_0}D_z + \partial_x H_y - \partial_y H_x, \\ \text{(vi)} & \partial_t E_z &= -\dfrac{1}{\epsilon_0}\sigma_y E_z + \dfrac{1}{\epsilon_0}\partial_t D_z. \end{array}\right. \tag{4.4}$$

We can rewrite (4.4) in vector form as

$$\left\{\begin{array}{rcl} \partial_t \mathbf{B} &=& -\dfrac{1}{\epsilon_0}\Sigma_2 \mathbf{B} \;-\; \overrightarrow{\operatorname{curl}}\, E, \\ \partial_t \mathbf{H} &=& \dfrac{1}{\mu_0}\partial_t \mathbf{B} \;+\; \dfrac{1}{\epsilon_0\mu_0}\Sigma_1 \mathbf{B}, \\ \partial_t D &=& -\dfrac{1}{\epsilon_0}\sigma_x D \;+\; \operatorname{curl}\mathbf{H}, \\ \partial_t E &=& -\dfrac{1}{\epsilon_0}\sigma_y E \;+\; \dfrac{1}{\epsilon_0}\partial_t D. \end{array}\right. \tag{4.5}$$

In the above $\mathbf{H} = (H_x, H_y)$, $\mathbf{B} = (B_x, B_y)$, $E = E_z$ and $D = D$. In (4.5)

$$\Sigma_1 = \begin{pmatrix} \sigma_x & 0 \\ 0 & \sigma_y \end{pmatrix}; \quad \Sigma_2 = \begin{pmatrix} \sigma_y & 0 \\ 0 & \sigma_x \end{pmatrix}. \tag{4.6}$$

Let $\mathbb{D}$ denote the computational domain in $\mathbb{R}^2$. We denote the domain $\mathbb{D}$ including the surrounding finite PML layers by Ω. In (4.5), the operators denoted by $\overrightarrow{\operatorname{curl}}$, and curl are

linear differential operators which are defined as

$$\overrightarrow{\text{curl}}\,\phi = (\partial_y\phi, -\partial_x\phi),\ \text{curl}\,\mathbf{v} = \partial_x v_y - \partial_y v_x,\ \ \forall\ \mathbf{v} = (v_x, v_y) \in \mathcal{D}'(\Omega)^2,\ \forall\ \phi \in \mathcal{D}'(\Omega). \quad (4.7)$$

Here $\mathcal{D}'(\Omega)$ is the space of distributions on Ω. The operator curl appears as the (formal) transpose of the operator $\overrightarrow{\text{curl}}$ [15], i.e.,

$$\langle \text{curl}\,\mathbf{v}, \phi\rangle = \langle \mathbf{v}, \overrightarrow{\text{curl}}\,\phi\rangle,\ \forall \mathbf{v} \in \mathcal{D}'(\Omega)^2,\ \phi \in \mathcal{D}'(\Omega). \quad (4.8)$$

Thus, the PML model consists in solving system (4.4) (or (4.5)) for the six variables B_x, B_y, H_x, H_y, D_z, E_z in Ω, with PEC conditions on $\partial\Omega$ to terminate the PML; namely, $\mathbf{n} \times \mathbf{E} = 0$, on $\partial\Omega$, where $\mathbf{n}$ is the outward unit normal to $\partial\Omega$. In the case of the 2D TM mode the PEC condition translates to $E = E_z = 0$, on $\partial\Omega$. We also have the initial conditions

$$E(x,0) = E_0, \quad D(x,0) = E_0, \quad \mathbf{H}(x,0) = \mathbf{H}_0, \quad \mathbf{B}(x,0) = \mathbf{H}_0, \quad \text{for} \quad x \in \Omega. \quad (4.9)$$

We consider the following variational formulation of system (4.5) which is suitable for discretization by finite elements.

Find $(E(\cdot,t), D(\cdot,t), \mathbf{H}(\cdot,t), \mathbf{B}(\cdot,t)) \in H_0^1(\Omega) \times H_0^1(\Omega) \times [\text{L}^2(\Omega)]^2 \times [\text{L}^2(\Omega)]^2$ such that for all $\mathbf{\Psi} \in [\text{L}^2(\Omega)]^2$, for all $\phi \in H_0^1(\Omega)$,

$$\left\{\begin{array}{rcl} \dfrac{d}{dt}\displaystyle\int_\Omega \mathbf{B}\cdot\mathbf{\Psi}\ d\mathbf{x} &=& -\dfrac{1}{\epsilon_0}\displaystyle\int_\Omega \Sigma_2\mathbf{B}\cdot\mathbf{\Psi}\ d\mathbf{x} - \displaystyle\int_\Omega \overrightarrow{\text{curl}}\,E\cdot\mathbf{\Psi}\ d\mathbf{x}, \\ \dfrac{d}{dt}\displaystyle\int_\Omega \mathbf{H}\cdot\mathbf{\Psi}\ d\mathbf{x} &=& \dfrac{1}{\mu_0}\dfrac{d}{dt}\displaystyle\int_\Omega \mathbf{B}\cdot\mathbf{\Psi}\ d\mathbf{x} + \dfrac{1}{\epsilon_0\mu_0}\displaystyle\int_\Omega \Sigma_1\mathbf{B}\cdot\mathbf{\Psi}\ d\mathbf{x}, \\ \dfrac{d}{dt}\displaystyle\int_\Omega D\cdot\phi\ d\mathbf{x} &=& -\dfrac{1}{\epsilon_0}\displaystyle\int_\Omega \sigma_x D\cdot\phi\ d\mathbf{x} + \displaystyle\int_\Omega \overrightarrow{\text{curl}}\,\phi\cdot\mathbf{H}\ d\mathbf{x}, \\ \dfrac{d}{dt}\displaystyle\int_\Omega E\cdot\phi\ d\mathbf{x} &=& -\dfrac{1}{\epsilon_0}\displaystyle\int_\Omega \sigma_y E\cdot\phi\ d\mathbf{x} + \dfrac{1}{\epsilon_0}\dfrac{d}{dt}\displaystyle\int_\Omega D\cdot\phi\ d\mathbf{x}. \end{array}\right. \quad (4.10)$$

We assume that the fields $(E, D, \mathbf{H}, \mathbf{B})$ are sufficiently differentiable in time. We note that, for $E \in \text{L}^2(\Omega)$, $\overrightarrow{\text{curl}}\,E = (\partial_y E, -\partial_x E) \in [\text{L}^2(\Omega)]^2$ implies that both the partial derivatives of E must be in $\text{L}^2(\Omega)$. Hence we must have $E \in H^1(\Omega)$.

5 Energy Estimates for the UPML

Maxwell's equations form a symmetric hyperbolic system. The solution to such a system is strongly well-posed [21]. It is natural then to consider the well-posedness of the different PML

models. Abarbanel and Gottlieb [1] showed that Berenger's split-field PML is a weakly well-posed system; thus instabilities could appear in numerical implementations of this model. In [29] the authors demonstrate that the Zhao-Cangellaris's model for the PML is strongly well-posed. Bécache and Joly [4] show this well-posedness explicitly by presenting energy decay results for the 2D TE mode of this model.

We derive energy decay results for the 2D TM mode of the UPML in two cases; σ a positive constant and $\sigma \in L^\infty(\Omega)$. We have derived estimates for the UPML model under the same conditions as done in [4] for the Zhao-Cangellaris model. The Zhao-Cangellaris's model established the equivalence between the Chew-Weedon's PML model [11] based on coordinate stretching and the anisotropic model by Sacks *et al.*. As a consequence, the energy decay results for the Zhao-Cangellaris's PML and the UPML appear to be similar. This is to be understood in the sense that the definitions of the energies involved are identical in the second, third, and fourth estimate and almost identical in the first estimate.

To simplify the analysis, we assume that $\epsilon_0 = \mu_0 = 1$ in the rest of this section. We also assume that we start with zero initial conditions in (4.9). Let $(\cdot, \cdot)$ denote the $\mathrm{L}^2(\Omega)$ inner product and $||\cdot||_{\mathrm{L}^2(\Omega)}$ the corresponding norm.

Energy Estimate 1 *Let us assume that the computational domain $\mathbb{D}$ has a PML in the region $x > 0$. In this case, $\sigma_x = \sigma$ and $\sigma_y = 0$. For a positive constant value of σ, the energy $\mathcal{E}_1^x$ of the PML system defined as*

$$\mathcal{E}_1^x = \frac{1}{2}\left(\|\partial_t H_x\|^2_{\mathrm{L}^2(\Omega)} + \|\partial_t H_y\|^2_{\mathrm{L}^2(\Omega)} + \|\sigma B_y\|^2_{\mathrm{L}^2(\Omega)} + \|(\partial_t + \sigma)\, E\|^2_{\mathrm{L}^2(\Omega)}\right), \tag{5.1}$$

is a decreasing function of time. It satisfies the identity

$$\frac{d}{dt}\mathcal{E}_1^x = -2\sigma \|\partial_t H_y\|^2_{\mathrm{L}^2(\Omega)} \leq 0. \tag{5.2}$$

Proof. Consider (4.4), with $\sigma_x = \sigma$ and $\sigma_y = 0$. Applying the operator $(\partial_t + \sigma)$ to (4.4, i), the operator ∂_t to (4.4, ii) and combining the two results, we get

$$\partial_t^2 H_x = -\partial_y (\partial_t + \sigma)\, E. \tag{5.3}$$

We note that, since σ is a constant, the operator $(\partial_t + \sigma)$ commutes with the operators ∂_y and ∂_x. Taking the inner product of both sides of (5.3) with $\partial_t H_x$ we have

$$\frac{1}{2}\frac{d}{dt}\|\partial_t H_x\|^2_{\mathrm{L}^2(\Omega)} = -\left(\partial_y (\partial_t + \sigma)\, E, \partial_t H_x\right). \tag{5.4}$$

Next, apply the operator $(\partial_t + \sigma)$ to (4.4, iii) to get

$$(\partial_t + \sigma)^2 B_y = (\partial_t + \sigma)\, \partial_x E. \tag{5.5}$$

Taking inner products on both sides of (5.5) with $\partial_t B_y$ we get

$$\left(\partial_t^2 B_y, \partial_t B_y\right) + 2\sigma \left(\partial_t B_y, \partial_t B_y\right) + \sigma^2 \left(B_y, \partial_t B_y\right) = \left((\partial_t + \sigma)\, \partial_x E, \partial_t B_y\right). \tag{5.6}$$

From (4.4, iv), using $\partial_t B_y = \partial_t H_y$ in (5.6), we have

$$\frac{1}{2}\frac{d}{dt}\left\|\partial_t H_y\right\|^2_{\mathrm{L}^2(\Omega)} + 2\sigma \left(\partial_t H_y, \partial_t H_y\right) + \frac{1}{2}\frac{d}{dt}\left\|\sigma B_y\right\|^2_{\mathrm{L}^2(\Omega)} = \left(\partial_x \left(\partial_t + \sigma\right) E, \partial_t H_y\right). \tag{5.7}$$

Finally, to eliminate D, we apply the operator ∂_t to (4.4, v) and the operator $(\partial_t + \sigma)$ to (4.4, vi), combining the results to get

$$(\partial_t + \sigma)\, \partial_t E = \partial_t \partial_x H_y - \partial_t \partial_y H_x. \tag{5.8}$$

Taking the inner products of both sides of (5.8) with $(\partial_t + \sigma)\, E$, we have

$$\frac{1}{2}\frac{d}{dt}\left\|(\partial_t + \sigma)\, E\right\|^2_{\mathrm{L}^2(\Omega)} = \left(\partial_t \partial_x H_y, (\partial_t + \sigma)\, E\right) - \left(\partial_t \partial_y H_x, (\partial_t + \sigma)\, E\right). \tag{5.9}$$

Integrating by parts in the right hand side of (5.9) we have

$$\frac{1}{2}\frac{d}{dt}\left\|(\partial_t + \sigma)\, E\right\|^2_{\mathrm{L}^2(\Omega)} = -\left(\partial_t H_y, \partial_x \left(\partial_t + \sigma\right) E\right) + \left(\partial_t H_x, \partial_y \left(\partial_t + \sigma\right) E\right). \tag{5.10}$$

Adding (5.4), (5.7) and (5.10) and using definition (5.1) of $\mathcal{E}_1^x$ we have

$$\frac{d}{dt}\mathcal{E}_1^x + 2\sigma \left\|\partial_t H_y\right\|^2_{\mathrm{L}^2(\Omega)} = 0. \tag{5.11}$$

As $\sigma > 0$ we obtain (5.2) from (5.11). This implies that $\mathcal{E}_1^x$ is a decreasing function of time. ■

Energy Estimate 2 *Let the computational domain $\mathbb{D}$ be surrounded by PML's on all sides (see Figure 1). Consider a corner region of two overlapping layers in which both σ_x and σ_y are positive and constants. The solution of the UPML TM mode satisfies the energy inequality*

$$\mathcal{E}_2^C(t) \le \mathcal{E}_2^C(s), \quad \textit{for all} \quad t \ge s, \tag{5.12}$$

where $\mathcal{E}_2^C$ is the second order energy defined as

$$\mathcal{E}_2^C(t) = \frac{1}{2}\left(\left\|\partial_t^2 \mathbf{H}\right\|^2_{\mathrm{L}^2(\Omega)} + \left\|\Sigma_2 \partial_t \mathbf{H}\right\|^2_{\mathrm{L}^2(\Omega)} + \left\|(\partial_t + \sigma_x)\left(\partial_t + \sigma_y\right) E\right\|^2_{\mathrm{L}^2(\Omega)}\right). \tag{5.13}$$

Proof. The UPML model for this case is

$$\begin{cases} \text{(i)} & \partial_t \mathbf{B} + \Sigma_2 \mathbf{B} &=& -\overrightarrow{\operatorname{curl}}\, E, \\ \text{(ii)} & \partial_t \mathbf{B} + \Sigma_1 \mathbf{B} &=& \partial_t \mathbf{H}, \\ \text{(iii)} & (\partial_t + \sigma_x)\, D &=& \operatorname{curl} \mathbf{H}, \\ \text{(iv)} & (\partial_t + \sigma_y)\, E &=& \partial_t D. \end{cases} \tag{5.14}$$

We eliminate $\mathbf{B}$ from (5.14, i) and (5.14, ii) by applying the operator $(\partial_t + \Sigma_2)$ to (5.14, ii) and the operator $(\partial_t + \Sigma_1)$ to (5.14, i) and combine the results to get

$$\partial_t \left(\partial_t + \Sigma_2\right) \mathbf{H} = -\left(\partial_t + \Sigma_1\right) \overrightarrow{\operatorname{curl}}\, E. \tag{5.15}$$

Applying the operator $(\partial_t + \Sigma_2)$ to both sides in the equation above, we get

$$\partial_t \left(\partial_t + \Sigma_2\right)^2 \mathbf{H} = -\left(\partial_t + \Sigma_2\right)\left(\partial_t + \Sigma_1\right) \overrightarrow{\operatorname{curl}}\, E. \tag{5.16}$$

Taking the inner product of both sides with $\partial_t^2 \mathbf{H}$ we have

$$\left(\partial_t \left(\partial_t + \Sigma_2\right)^2 \mathbf{H}, \partial_t^2 \mathbf{H}\right) = -\left(\left(\partial_t + \Sigma_2\right)\left(\partial_t + \Sigma_1\right) \overrightarrow{\operatorname{curl}}\, E, \partial_t^2 \mathbf{H}\right). \tag{5.17}$$

This implies

$$\begin{aligned} \frac{1}{2}\frac{d}{dt}\left(\left\|\partial_t^2 \mathbf{H}\right\|_{\mathrm{L}^2(\Omega)}^2 + \left\|\Sigma_2 \partial_t \mathbf{H}\right\|_{\mathrm{L}^2(\Omega)}^2\right) + 2\Sigma_2 \left\|\partial_t^2 \mathbf{H}\right\|_{\mathrm{L}^2(\Omega)}^2 \\ = -\left(\left(\partial_t + \Sigma_2\right)\left(\partial_t + \Sigma_1\right) \overrightarrow{\operatorname{curl}}\, E, \partial_t^2 \mathbf{H}\right) \end{aligned} \tag{5.18}$$

Next, to eliminate D we apply the operator ∂_t to (5.14, iii), and the operator $(\partial_t + \sigma_x)$ to (5.14, iv), and combine the results to get

$$\left(\partial_t + \sigma_x\right)\left(\partial_t + \sigma_y\right) E = \partial_t \operatorname{curl} \mathbf{H}. \tag{5.19}$$

Applying ∂_t to both sides of the above equation and taking inner products with $\left(\partial_t + \sigma_x\right)\left(\partial_t + \sigma_y\right) E$, we get

$$\left(\partial_t \left(\partial_t + \sigma_x\right)\left(\partial_t + \sigma_y\right) E, \left(\partial_t + \sigma_x\right)\left(\partial_t + \sigma_y\right) E\right) = \left(\partial_t^2 \operatorname{curl} \mathbf{H}, \left(\partial_t + \sigma_x\right)\left(\partial_t + \sigma_y\right) E\right). \tag{5.20}$$

This implies

$$\frac{1}{2}\frac{d}{dt}\left\|\left(\partial_t + \sigma_x\right)\left(\partial_t + \sigma_y\right) E\right\|_{\mathrm{L}^2(\Omega)}^2 = \left(\partial_t^2 \operatorname{curl} \mathbf{H}, \left(\partial_t + \sigma_x\right)\left(\partial_t + \sigma_y\right) E\right). \tag{5.21}$$

Integrating the right hand side by parts and making use of the fact that the operators $(\partial_t + \sigma_x)$ and $(\partial_t + \sigma_y)$ commute, we have

$$\frac{1}{2}\frac{d}{dt}\left\|\left(\partial_t + \sigma_x\right)\left(\partial_t + \sigma_y\right)E\right\|^2_{\mathrm{L}^2(\Omega)} = \left(\partial_t^2\mathbf{H}, \left(\partial_t + \Sigma_2\right)\left(\partial_t + \Sigma_1\right)\overrightarrow{\mathrm{curl}}\, E\right). \tag{5.22}$$

Adding (5.18) and (5.22), using the definition of the energy $\mathcal{E}_2^C$, and as $\sigma_x > 0$ and $\sigma_y > 0$, we have

$$\frac{d}{dt}\mathcal{E}_2^C(t) = -2\Sigma_2\left\|\partial_t^2\mathbf{H}\right\|^2_{\mathrm{L}^2(\Omega)} < 0, \tag{5.23}$$

which implies that $\mathcal{E}_2^C$ is a decreasing function of time. Thus, (5.12) is proved. ■

Energy Estimate 3 *Again, assume a PML in the region $x > 0$. For $\sigma \in L^\infty(\Omega)$, the zero order energy $\mathcal{E}_0^x$ of the UPML defined by*

$$\mathcal{E}_0^x(t) = \frac{1}{2}\left(\|H_x\|^2_{\mathrm{L}^2(\Omega)} + \|H_y\|^2_{\mathrm{L}^2(\Omega)} + \|E\|^2_{\mathrm{L}^2(\Omega)} + \|H_x - B_x\|^2_{\mathrm{L}^2(\Omega)}\right), \tag{5.24}$$

satisfies the energy estimate

$$\mathcal{E}_0^x(t) \le \mathcal{E}_0^x(0) + 2\|\sigma\|_\infty \int_0^t \mathcal{E}_0^x(s)ds. \tag{5.25}$$

Proof. Consider (4.4), with $\sigma_x = \sigma$ and $\sigma_y = 0$. Taking the inner product of both sides of (4.4, i) with H_x, both sides of (4.4, iii) with H_y, both sides of (4.4, v) with E, adding the three resulting equations and integrating the right hand side by parts (IBP) we get

$$\begin{aligned}&(\partial_t B_x, H_x) + ((\partial_t + \sigma)B_y, H_y) + ((\partial_t + \sigma)D, E) = \\ &\quad -(\partial_y E, H_x) + (\partial_x E, H_y) + (\partial_x H_y - \partial_y H_x, E) = 0 \quad \text{(by IBP)}.\end{aligned} \tag{5.26}$$

Assuming that we start from zero initial conditions, from (4.4, ii, iv, vi), we have

$$\begin{cases} \text{(i)} & H_x(\cdot,t) = B_x(\cdot,t) + \sigma\tilde{B}_x(\cdot,t), \\ \text{(ii)} & H_y(\cdot,t) = B_y(\cdot,t), \\ \text{(iii)} & E(\cdot,t) = D(\cdot,t), \end{cases} \tag{5.27}$$

where, in the above

$$\tilde{B}_x(\cdot,t) = \int_0^t B_x(\cdot,s)\ \mathrm{ds}. \tag{5.28}$$

From (5.27, ii), we have

$$((\partial_t + \sigma)B_y, H_y) = (\partial_t H_y, H_y) + (\sigma H_y, H_y) = \frac{1}{2}\frac{d}{dt}\|H_y\|^2_{\mathrm{L}^2(\Omega)} + (\sigma H_y, H_y). \tag{5.29}$$

Next, from (5.27, iii), we have

$$((\partial_t + \sigma)D, E) = (\partial_t E, E) + (\sigma E, E) = \frac{1}{2}\frac{d}{dt}\|E\|^2_{\mathrm{L}^2(\Omega)} + (\sigma E, E)\,. \tag{5.30}$$

Finally, from (4.4, ii), we have

$$(\partial_t B_x, H_x) = (\partial_t H_x - \sigma B_x, H_x) = (\partial_t H_x, H_x) - (\sigma B_x, H_x)\,. \tag{5.31}$$

Using (5.27, i), we obtain

$$\begin{aligned}(\partial_t B_x, H_x) &= \frac{1}{2}\frac{d}{dt}\|H_x\|^2_{\mathrm{L}^2(\Omega)} - \left(\sigma(H_x - \sigma\tilde{B}_x), H_x\right)\\ &= \frac{1}{2}\frac{d}{dt}\|H_x\|^2_{\mathrm{L}^2(\Omega)} - (\sigma H_x, H_x) + \left(\sigma^2\tilde{B}_x, H_x\right).\end{aligned} \tag{5.32}$$

The last term in (5.32) can be rewritten using (5.27, i), (4.4, ii) and rearranging terms as

$$\begin{aligned}\left(\sigma^2\tilde{B}_x, H_x\right) &= (\sigma(H_x - B_x), H_x)\\ &= (\sigma(H_x - B_x), H_x - B_x) + (\partial_t(H_x - B_x), H_x - B_x)\,.\end{aligned} \tag{5.33}$$

Using (5.33) in (5.32) we get

$$\begin{aligned}(\partial_t B_x, H_x) = \frac{1}{2}\frac{d}{dt}&\left(\|H_x\|^2_{\mathrm{L}^2(\Omega)} + \|H_x - B_x\|^2_{\mathrm{L}^2(\Omega)}\right)\\ &- (\sigma H_x, H_x) + (\sigma(H_x - B_x), H_x - B_x)\,.\end{aligned} \tag{5.34}$$

Substituting (5.29), (5.30) and (5.34) in (5.26) we have

$$\begin{aligned}&\frac{1}{2}\frac{d}{dt}\left(\|H_x\|^2_{\mathrm{L}^2(\Omega)} + \|H_y\|^2_{\mathrm{L}^2(\Omega)} + \|E\|^2_{\mathrm{L}^2(\Omega)} + \|H_x - B_x\|^2_{\mathrm{L}^2(\Omega)}\right)\\ &= (\sigma H_x, H_x) - (\sigma H_y, H_y) - (\sigma E, E) - (\sigma(H_x - B_x), H_x - B_x).\end{aligned} \tag{5.35}$$

The right hand side of (5.35) can be bounded as

$$\begin{aligned}&(\sigma H_x, H_x) - (\sigma H_y, H_y) - (\sigma E, E) - (\sigma(H_x - B_x), H_x - B_x)\\ &\leq 2\|\sigma\|_\infty\{\frac{1}{2}\left(\|H_x\|^2_{\mathrm{L}^2(\Omega)} + \|H_y\|^2_{\mathrm{L}^2(\Omega)} + \|E\|^2_{\mathrm{L}^2(\Omega)} + \|H_x - B_x\|^2_{\mathrm{L}^2(\Omega)}\right)\} = 2\|\sigma\|_\infty\,\mathcal{E}^x_0,\end{aligned} \tag{5.36}$$

where, $\mathcal{E}^x_0$ is defined in (5.24). Thus, from (5.24), (5.35) and (5.36) we have

$$\frac{d}{dt}\mathcal{E}^x_0(t) \leq 2\|\sigma\|_\infty\,\mathcal{E}^x_0(t) \implies \mathcal{E}^x_0(t) \leq \mathcal{E}^x_0(0) + 2\|\sigma\|_\infty\int_0^t \mathcal{E}^x_0(s)\,\mathrm{ds}. \tag{5.37}$$

■

Energy Estimate 4 *Let the computational domain $\mathbb{D}$ be surrounded by PML's on all sides (see Figure 1). Consider a corner region of two overlapping layers in which both σ_x and σ_y are in $L^\infty(\Omega)$. If the product $\sigma_x\sigma_y$ remains positive everywhere in the domain of interest then the zero order energy of the UPML given by*

$$\mathcal{E}_0^C(t) = \frac{1}{2}\left(\|\mathbf{H}-\mathbf{B}\|^2_{\mathrm{L}^2(\Omega)} + \|E\|^2_{\mathrm{L}^2(\Omega)} + \|\mathbf{H}\|^2_{\mathrm{L}^2(\Omega)} + \left(\sigma_x\sigma_y\tilde{E},\tilde{E}\right)\right), \tag{5.38}$$

where $\tilde{E}(t) = \displaystyle\int_0^t E(\cdot,s)ds$, *satisfies the energy estimate*

$$\mathcal{E}_0^C(t) \le \mathcal{E}_0^C(0) + 3\left(\|\sigma_x\|_\infty + \|\sigma_y\|_\infty\right)\int_0^t \mathcal{E}_0^C(s)ds. \tag{5.39}$$

Proof. The UPML equations in this case are given by (5.14). From (5.14, i, iii), we get after integrating by parts,

$$((\partial_t+\Sigma_2)\mathbf{B},\mathbf{H}) + ((\partial_t+\sigma_x)D,E) = -\left(\overrightarrow{\mathrm{curl}}\,E,\mathbf{H}\right) + (\mathrm{curl}\,\mathbf{H},E) = 0. \tag{5.40}$$

Consider the term

$$((\partial_t+\sigma_x)D,E) = (\partial_t D,E) + (\sigma_x D,E). \tag{5.41}$$

From (5.14, iv), assuming zero initial conditions we have

$$D(\cdot,t) = E(\cdot,t) + \sigma_y\tilde{E}(\cdot,t). \tag{5.42}$$

Thus, from (5.41) and (5.42) we have

$$\begin{aligned}((\partial_t+\sigma_x)D,E) &= (\partial_t E,E) + (\sigma_x E,E) + (\sigma_y E,E) + \left(\sigma_x\sigma_y\tilde{E},E\right)\\ &= \frac{1}{2}\frac{d}{dt}\|E\|^2_{\mathrm{L}^2(\Omega)} + \frac{1}{2}\frac{d}{dt}\left(\sigma_x\sigma_y\tilde{E},\tilde{E}\right) + ((\sigma_x+\sigma_y)E,E).\end{aligned} \tag{5.43}$$

From, (5.14, ii), we have

$$\mathbf{H}(\cdot,t) = \mathbf{B}(\cdot,t) + \Sigma_1\tilde{\mathbf{B}}(\cdot,t), \tag{5.44}$$

where

$$\tilde{\mathbf{B}}(\cdot,t) = \int_0^t \mathbf{B}(\cdot,s)\ \mathrm{ds} \tag{5.45}$$

From, (5.44) and (5.45) we get

$$\begin{aligned}((\partial_t+\Sigma_2)\mathbf{B},\mathbf{H}) &= (\partial_t\mathbf{H},\mathbf{H}) + ((\sigma_y-\sigma_x)B_x,H_x) + ((\sigma_x-\sigma_y)B_y,H_y)\\ &= \frac{1}{2}\frac{d}{dt}\|\mathbf{H}\|^2_{\mathrm{L}^2(\Omega)} + (\Sigma_2\mathbf{B},\mathbf{H}) - (\Sigma_1\mathbf{B},\mathbf{H}).\end{aligned} \tag{5.46}$$

Again, from (5.44) and (5.45) we get

$$\begin{aligned}(\Sigma_1\mathbf{B},\mathbf{H}) &= (\sigma_x B_x, H_x) + (\sigma_y B_y, H_y)\\ &= \left(\sigma_x(H_x - \sigma_x\tilde{B}_x), H_x\right) + \left(\sigma_y(H_y - \sigma_y\tilde{B}_y), H_y\right)\\ &= (\sigma_x H_x, H_x) + (\sigma_y H_y, H_y) - \left(\sigma_x^2\tilde{B}_x, H_x\right) - \left(\sigma_y^2\tilde{B}_y, H_y\right)\\ &= (\Sigma_1\mathbf{H},\mathbf{H}) - \left(\sigma_x^2\tilde{B}_x, H_x\right) - \left(\sigma_y^2\tilde{B}_y, H_y\right).\end{aligned} \tag{5.47}$$

Using (5.47) in (5.46) we get

$$\begin{aligned}((\partial_t + \Sigma_2)\mathbf{B},\mathbf{H}) &= \frac{1}{2}\frac{d}{dt}\|\mathbf{H}\|^2_{\mathrm{L}^2(\Omega)} + (\Sigma_2\mathbf{B},\mathbf{H}) - (\Sigma_1\mathbf{H},\mathbf{H})\\ &\quad + \left(\sigma_x^2\tilde{B}_x, H_x\right) + \left(\sigma_y^2\tilde{B}_y, H_y\right)\\ &= \frac{1}{2}\frac{d}{dt}\|\mathbf{H}\|^2_{\mathrm{L}^2(\Omega)} + (\Sigma_2\mathbf{B},\mathbf{H}) - (\Sigma_1\mathbf{H},\mathbf{H}) + \left(\Sigma_1^2\tilde{\mathbf{B}},\mathbf{H}\right).\end{aligned} \tag{5.48}$$

We can simplify the last term in (5.48) as follows

$$\begin{aligned}\left(\Sigma_1^2\tilde{\mathbf{B}},\mathbf{H}\right) &= (\Sigma_1(\mathbf{H}-\mathbf{B}),\mathbf{H}-\mathbf{B}) + (\Sigma_1\mathbf{H},\mathbf{B}) + (\partial_t(\mathbf{H}-\mathbf{B}),\mathbf{H}-\mathbf{B}) - (\Sigma_1\mathbf{B},\mathbf{H})\\ &= \frac{1}{2}\frac{d}{dt}\|\mathbf{H}-\mathbf{B}\|^2_{\mathrm{L}^2(\Omega)} + (\Sigma_1(\mathbf{H}-\mathbf{B}),\mathbf{H}-\mathbf{B}).\end{aligned} \tag{5.49}$$

Also

$$(\Sigma_2\mathbf{B},\mathbf{H}) = (\Sigma_2(\mathbf{B}-\mathbf{H}),\mathbf{H}) + (\Sigma_2\mathbf{H},\mathbf{H}). \tag{5.50}$$

From (5.48), (5.49), and (5.50) we have

$$\begin{aligned}((\partial_t + \Sigma_2)\mathbf{B},\mathbf{H}) &= \frac{1}{2}\frac{d}{dt}\left(\|\mathbf{H}\|^2_{\mathrm{L}^2(\Omega)} + \|\mathbf{H}-\mathbf{B}\|^2_{\mathrm{L}^2(\Omega)}\right) + (\Sigma_2(\mathbf{B}-\mathbf{H}),\mathbf{H})\\ &\quad + ((\Sigma_2-\Sigma_1)\mathbf{H},\mathbf{H}) + (\Sigma_1(\mathbf{H}-\mathbf{B}),\mathbf{H}-\mathbf{B})\end{aligned} \tag{5.51}$$

From (5.43) and (5.51) we have

$$\begin{aligned}((\partial_t + \sigma_x)D, E) + ((\partial_t + \Sigma_2)\mathbf{B},\mathbf{H}) &= (\Sigma_1(\mathbf{H}-\mathbf{B}),\mathbf{H}-\mathbf{B})\\ &\quad + \frac{1}{2}\frac{d}{dt}\left(\|E\|^2_{\mathrm{L}^2(\Omega)} + \|\mathbf{H}\|^2_{\mathrm{L}^2(\Omega)} + \|\mathbf{H}-\mathbf{B}\|^2_{\mathrm{L}^2(\Omega)} + \left(\sigma_x\sigma_y\tilde{E},\tilde{E}\right)\right)\\ &\quad + ((\sigma_x+\sigma_y)E, E) + (\Sigma_2(\mathbf{B}-\mathbf{H}),\mathbf{H}) + ((\Sigma_2-\Sigma_1)\mathbf{H},\mathbf{H}) = 0.\end{aligned} \tag{5.52}$$

Using the definition of the energy $\mathcal{E}_0^C$ in (5.38) we have

$$\begin{aligned}\frac{d}{dt}\mathcal{E}_0^C &= ((\Sigma_1-\Sigma_2)\mathbf{H},\mathbf{H}) - (\Sigma_1(\mathbf{H}-\mathbf{B}),\mathbf{H}-\mathbf{B}) - ((\sigma_x+\sigma_y)E,E)\\ &\quad + (\Sigma_2(\mathbf{H}-\mathbf{B}),\mathbf{H}).\end{aligned} \tag{5.53}$$

We can bound the terms on the right hand hand of (5.53) as follows. We have

$$\begin{aligned}&(\Sigma_2(\mathbf{H}-\mathbf{B}),\mathbf{H})+((\Sigma_1-\Sigma_2)\mathbf{H},\mathbf{H})\\ &\leq\ \{\|\sigma_x\|_\infty+\|\sigma_y\|_\infty\}\left[\frac{1}{2}\left(\|\mathbf{H}\|^2_{\mathrm{L}^2(\Omega)}+\|\mathbf{H}-\mathbf{B}\|^2_{\mathrm{L}^2(\Omega)}\right)+\|\mathbf{H}\|^2_{\mathrm{L}^2(\Omega)}\right].\end{aligned}\tag{5.54}$$

Substituting (5.54) in (5.53) we obtain

$$\begin{aligned}\frac{d}{dt}\mathcal{E}_0^C\ &\leq\ \{\|\sigma_x\|_\infty+\|\sigma_y\|_\infty\}\left[\|E\|^2_{\mathrm{L}^2(\Omega)}+\frac{3}{2}\|\mathbf{H}\|^2_{\mathrm{L}^2(\Omega)}+\frac{3}{2}\|\mathbf{H}-\mathbf{B}\|^2_{\mathrm{L}^2(\Omega)}\right]\\ &\leq 3\{\|\sigma_x\|_\infty+\|\sigma_y\|_\infty\}\mathcal{E}_0^C.\end{aligned}\tag{5.55}$$

Integrating, we thus have the energy estimate

$$\mathcal{E}_0^C(t)\leq\mathcal{E}_0^C(0)+3\left(\|\sigma_x\|_\infty+\|\sigma_y\|_\infty\right)\int_0^t\mathcal{E}_0^C(s)ds,\tag{5.56}$$

which is (5.39). ■

6 The Discrete Mixed Finite Element Scheme

6.1 Space Discretization

Let Ω be a union of rectangles defining a regular mesh $(\mathcal{T}_h)$ with square elements (K) of edge $h>0$ as in Figure 2. We consider the following approximation space for $\mathbf{H}$ and $\mathbf{B}$:

$$\mathcal{V}_h=\{\mathbf{\Psi}_h\in[L^2(\Omega)]^2|\ \forall K\in\mathcal{T}_h,\mathbf{\Psi}_h|_K\in RT_{[0]}\},\tag{6.1}$$

where, $RT_{[0]}=P_{10}\times P_{01}$, is the lowest order Raviart-Thomas space [31] and for $k_1,k_2\ \in\mathbb{N}\cup\{0\}$,

$$P_{k_1k_2}=\{p(x_1,x_2)|p(x_1,x_2)=\sum_{0\leq i\leq k_1}\sum_{0\leq j\leq k_2}a_{ij}x_1^ix_2^j\}.$$

The basis functions for H_x have unity value along an e_y and are zero over all other edges (see Figure 2). Similarly, the basis functions for H_y have unity value along an e_x edge and are zero over all other edges (see Figure 2).

The approximation space for E and D is chosen to be

$$\mathcal{U}_h=\{\phi_h\in H_0^1(\Omega)|\quad\forall K\in\mathcal{T}_h,\phi_h|_K\in Q_1\},\tag{6.2}$$

where the space $Q_1=P_{11}$. The basis functions for E have unity value at one node and are zero at all other nodes. Figure 2 shows the locations for the degrees of freedom for for the electric and magnetic fields.

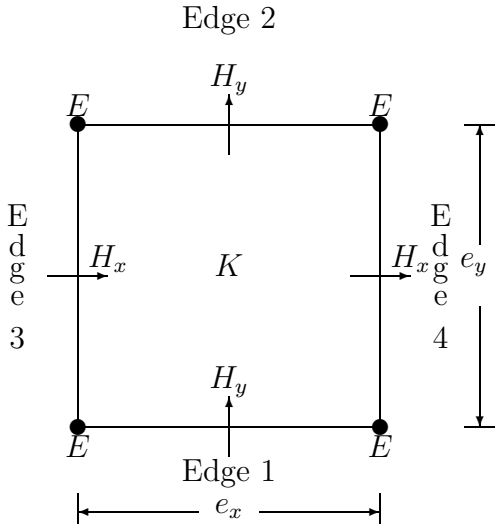

Figure 2: A sample domain element K. The degrees of freedom for the electric and magnetic fields are staggered in space. The degrees of freedom for the electric field E are at the nodes of the square. The degrees of freedom for H_x and H_y are at the midpoints of edges parallel to the x-axis and y-axis, respectively.

Based on the approximation spaces described above the space discrete scheme reads:

Find $(E_h(\cdot,t), D_h(\cdot,t), \mathbf{H}_h(\cdot,t), \mathbf{B}_h(\cdot,t)) \in \mathcal{U}_h \times \mathcal{U}_h \times \mathcal{V}_h \times \mathcal{V}_h$ such that for all $\mathbf{\Psi}_h \in \mathcal{V}_h$, for all $\phi_h \in \mathcal{U}_h$,

$$\left\{\begin{array}{rcl}
\dfrac{d}{dt}\displaystyle\int_\Omega \mathbf{B}_h \cdot \mathbf{\Psi}_h d\mathbf{x} &=& -\dfrac{1}{\epsilon_0}\displaystyle\int_\Omega \Sigma_1 \mathbf{B}_h \cdot \mathbf{\Psi}_h d\mathbf{x} \;-\; \displaystyle\int_\Omega \overrightarrow{\mathrm{curl}}\, E_h \cdot \mathbf{\Psi}_h d\mathbf{x}, \\
\dfrac{d}{dt}\displaystyle\int_\Omega \mathbf{H}_h \cdot \mathbf{\Psi}_h d\mathbf{x} &=& \dfrac{1}{\mu_0}\dfrac{d}{dt}\displaystyle\int_\Omega \mathbf{B}_h \cdot \mathbf{\Psi}_h d\mathbf{x} \;+\; \dfrac{1}{\epsilon_0\mu_0}\displaystyle\int_\Omega \Sigma_2 \mathbf{B}_h \cdot \mathbf{\Psi}_h d\mathbf{x}, \\
\dfrac{d}{dt}\displaystyle\int_\Omega D_h \cdot \phi_h \; d\mathbf{x} &=& -\dfrac{1}{\epsilon_0}\displaystyle\int_\Omega \sigma_x D_h \cdot \phi_h \; d\mathbf{x} \;+\; \displaystyle\int_\Omega \overrightarrow{\mathrm{curl}}\, \phi_h \cdot \mathbf{H}_h \; d\mathbf{x}, \\
\dfrac{d}{dt}\displaystyle\int_\Omega E_h \cdot \phi_h \; d\mathbf{x} &=& -\dfrac{1}{\epsilon_0}\displaystyle\int_\Omega \sigma_y E_h \cdot \phi_h \; d\mathbf{x} \;+\; \dfrac{1}{\epsilon_0}\dfrac{d}{dt}\displaystyle\int_\Omega D_h \cdot \phi_h \; d\mathbf{x}.
\end{array}\right. \tag{6.3}$$

6.2 Time Discretization

For the time discretization we use a centered second order accurate finite difference scheme. For $k \in \mathbb{Z}$ let,

$$D_{\Delta t} V^k = \frac{V^{k+1/2} - V^{k-1/2}}{\Delta t}, \quad \overline{V}^k = \frac{V^{k+1/2} + V^{k-1/2}}{2}. \tag{6.4}$$

Using the definitions (6.4) we can describe the fully discrete scheme in space and time as:

Find $(E_h^{n+1}, D_h^{n+1}, \mathbf{H}_h^{n+\frac{1}{2}}, \mathbf{B}_h^{n+\frac{1}{2}}) \in \mathcal{U}_h \times \mathcal{U}_h \times \mathcal{V}_h \times \mathcal{V}_h$ such that for all $\mathbf{\Psi}_h \in \mathcal{V}_h$, for all $\phi_h \in \mathcal{U}_h$,

$$\left\{\begin{array}{llcll} \text{(i)} & (D_{\Delta t}\mathbf{B}_h^n, \mathbf{\Psi_h}) & = & -\frac{1}{\epsilon_0}(\Sigma_2\overline{\mathbf{B}_h^n}, \mathbf{\Psi}_h) & - \quad (\overrightarrow{\text{curl}}\, E_h^n\ ,\ \mathbf{\Psi}_h), \\ \text{(ii)} & (D_{\Delta t}\mathbf{H}_h^n, \mathbf{\Psi}_h) & = & \frac{1}{\mu_0}(D_{\Delta t}\mathbf{B}_h^n, \mathbf{\Psi}_h) & + \quad \frac{1}{\epsilon_0\mu_0}(\Sigma_1\overline{\mathbf{B}_h^n}, \mathbf{\Psi}_h), \\ \text{(iii)} & (D_{\Delta t}D_h^{n+\frac{1}{2}}, \phi_h) & = & -\frac{1}{\epsilon_0}(\sigma_x\overline{D_h}^{n+\frac{1}{2}}, \phi_h) & + \quad (\overrightarrow{\text{curl}}\, \phi_h, \mathbf{H}_h^{n+\frac{1}{2}}), \\ \text{(iv)} & (D_{\Delta t}E_h^{n+\frac{1}{2}}, \phi_h) & = & -\frac{1}{\epsilon_0}(\sigma_y\overline{E_h}^{n+\frac{1}{2}}, \phi_h) & + \quad \frac{1}{\epsilon_0}(D_{\Delta t}D_h^{n+\frac{1}{2}},\ \phi_h). \end{array}\right. \tag{6.5}$$

7 Analysis of the Discrete PML Model

The numerical approximation of time-dependent wave problems introduces errors which involve *dissipation*, *dispersion*, and *anisotropy*. The attenuation of the amplitude of the plane wave is referred to as dissipation. The mixed finite element scheme presented in Section 5.7 is a non-dissipative scheme for Maxwell's equations in free space [24]. However, the PML model, in which lower order terms are added, is a dissipative model. As seen in (2.13) waves are attenuated in the PML according to the distance of travel in a given direction.

The numerical model produces waves that propagate at incorrect speeds. The dependence of the velocity of propagation of the numerical sinusoidal waves on frequency is termed as dispersion, while the dependence of the velocity upon direction is referred to as numerical anisotropy. These errors are cumulative, which implies that, as waves propagate over long distances the numerical solution becomes corrupted and may completely deviate from the correct solution. A dispersive equation is one that admits plane wave solutions of the form $e^{i(\omega t - \mathbf{k}\cdot\mathbf{x})}$ for which the speed of propagation is dependent on the frequency. For time-harmonic waves, numerical dispersion results in the creation of a *phase error* in the solution. This is due to the incorrect modeling of the sinusoidal behavior of the propagating wave, as the piecewise polynomial approximation of a finite element method does not exactly match a sine or cosine function [23].

In this section we study the properties of the discrete PML model in terms of a numerical dispersion analysis which is performed on regular square elements. It describes the propagation of waves in the numerical method away from the boundaries. In addition, we also obtain information about the expected accuracy of the method. We also compare the stability and dispersion properties of the finite element method with those of the finite difference method

A study of the dispersion analysis of different mixed methods for the time domain Maxwell's equations is done in [27].

Recall that $\mathbf{k}$ denotes the wave vector for the continuous case. For simplicity, we again assume that $\epsilon_0 = \mu_0 = 1$, hence $c = 1$. We look for solutions to the continuous system (4.10), of the form

$$V(x, y, t) = V_0 \mathrm{e}^{\mathrm{i}\omega t - \mathbf{k}\cdot\mathbf{x}}, \tag{7.1}$$

where V is any one of E, D, H_x, H_y, B_x, B_y. Substituting (7.1) in (4.10) shows that ω and $\mathbf{k}$ are related by the dispersion relation

$$\omega^2 = \left(\frac{k_x}{s_x}\right)^2 + \left(\frac{k_y}{s_y}\right)^2 \tag{7.2}$$

Inside the computational domain, where $s_x = s_y = 1$, the dispersion relation is given by

$$\omega^2 = k_x^2 + k_y^2 = |\mathbf{k}|^2 \implies \omega = |\mathbf{k}|. \tag{7.3}$$

Other solutions are $\omega = 0$, or $\omega = -|\mathbf{k}|$. There are two types of velocities that are important here. The *phase velocity* is defined as

$$c = \frac{\omega}{|\mathbf{k}|}, \tag{7.4}$$

which in this case is 1, as we have assumed $\epsilon_0 = \mu_0 = c = 1$. The *group velocity* is defined to be

$$\mathbf{C}(\mathbf{k}) = \nabla_{\mathbf{k}}\omega(\mathbf{k}) = \frac{c\mathbf{k}}{|\mathbf{k}|}. \tag{7.5}$$

It is a well known fact, that the propagation of energy under dispersive partial differential equations is governed by the group velocity [35, 10, 36]. Asymptotically, the energy associated with the wave vector $\mathbf{k}$ moves at the *group speed* $|\mathbf{C}|$, which in the present case is $|\mathbf{C}| = 1$. Thus, regardless of the wave number $\mathbf{k}$, all plane waves move with the same group speed $|\mathbf{C}| = 1$.

7.1 Dispersion and Stability Analysis

We now perform a similar analysis for the semi-discrete system (6.3), where we consider exact integration in time. Let us assume an infinite PML in the region $x > 0$. Thus, $\sigma_y = 0$ and let $\sigma_x = \sigma$. We will look for solutions of the form

$$V(x, y, t) = \hat{V}(x, y)\mathrm{e}^{\mathrm{i}\omega t}, \tag{7.6}$$

to the semi-discrete system (6.3). Substituting (7.6) in (6.3), we obtain the time harmonic system

$$\begin{cases} \mathrm{i}\omega(\hat{B}_x, \psi_x) &= -\left(\partial_y \hat{E}, \psi_x\right), \\ \mathrm{i}\omega(\hat{H}_x, \psi_x) &= \mathrm{i}\omega\left(\left(1+\dfrac{\sigma}{i\omega}\right)\hat{B}_x, \psi_x\right), \\ \mathrm{i}\omega\left(\left(1+\dfrac{\sigma}{\mathrm{i}\omega}\right)\hat{B}_y, \psi_y\right) &= \left(\partial_x \hat{E}, \psi_y\right), \\ \mathrm{i}\omega(\hat{H}_y, \psi_y) &= \mathrm{i}\omega(\hat{B}_y, \psi_y), \\ \mathrm{i}\omega\left(\left(1+\dfrac{\sigma}{\mathrm{i}\omega}\right)\hat{D}, \phi\right) &= \left(\hat{H}_x, \partial_y \phi\right) - \left(\hat{H}_y, \partial_x \phi\right), \\ \mathrm{i}\omega(\hat{E}, \phi) &= \mathrm{i}\omega(\hat{D}, \phi). \end{cases} \tag{7.7}$$

We assume that σ is a piecewise constant function of x with jumps at $x = lh, l = 0, 1, 2, \ldots$, where $h = h_x = h_y$ is the mesh step size. Let

$$\sigma_l = \begin{cases} \text{Value of } \sigma \text{ on } (lh, (l+1)h), & \text{if } l \geq 0, \\ 0, & \text{if } l < 0. \end{cases} \tag{7.8}$$

Using the definition (3.3), we have

$$s_{x,l} = s_l = 1 + \frac{\sigma_l}{\mathrm{i}\omega}. \tag{7.9}$$

Since $\sigma_y = 0$, we have $s_y = 0$. As the PML is in the half space $x > 0$, $x = 0$ is the interface between the PML and the interior computation region. Let us define

$$\begin{cases} M_x u_{l,m} &= 4u_{l,m} + u_{l-1,m} + u_{l+1,m}, \\ M_y u_{l,m} &= 4u_{l,m} + u_{l,m-1} + u_{l,m+1}, \\ \tilde{S}_x u_{l,m} &= M_y u_{l-1/2,m} - M_y u_{l+1/2,m}, \\ \tilde{S}_y u_{l,m} &= M_x u_{l,m-1/2} - M_x u_{l,m+1/2}, \\ M_z u_{l,m} &= M_x M_y u_{l,m}. \end{cases} \tag{7.10}$$

Consider an interior super element as shown in Figure 3. Using the definitions (7.10) in (7.7), we obtain the following system of equations that corresponds to the space discrete

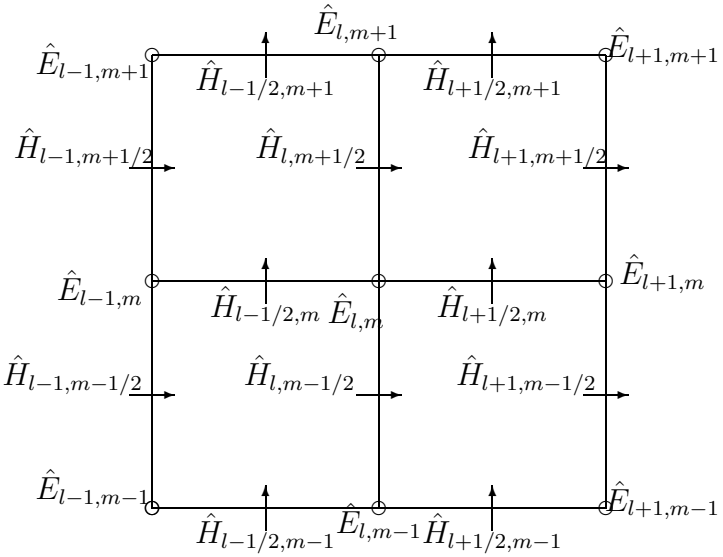

Figure 3: Dependency diagram for an interior super element.

finite element scheme (6.3):

$$\left\{\begin{array}{rcl} M_x\hat{B}_{l,m+1/2} & = & \dfrac{\mathrm{i}}{\omega h}M_x(\hat{E}_{l,m+1}-\hat{E}_{l,m}),\\ M_x\hat{H}_{l,m+1/2} & = & \left(\dfrac{s_l+s_{l-1}}{2}\right)M_x\hat{B}_{l,m+1/2},\\ s_lM_y\hat{B}_{l+1/2,m} & = & \dfrac{-\mathrm{i}}{\omega h}M_y(\hat{E}_{l+1,m}-\hat{E}_{l,m}),\\ M_y\hat{H}_{l+1/2,m} & = & M_y\hat{B}_{l+1/2,m},\\ \left(\dfrac{s_l+s_{l-1}}{2}\right)M_z\hat{D}_{l,m} & = & \dfrac{-6\mathrm{i}}{\omega h}(\tilde{S}_y\hat{H}_{l,m}-\tilde{S}_x\hat{H}_{l,m}),\\ M_z\hat{E}_{l,m} & = & M_z\hat{D}_{l,m}. \end{array}\right. \tag{7.11}$$

Combining the equations in (7.11), we obtain an equation in E by eliminating the other variables, which is

$$\begin{aligned} -\frac{\omega^2h^2}{6}\left(\frac{s_l+s_{l-1}}{2}\right)M_z\hat{E}_{l,m} &= \left(\frac{s_l+s_{l-1}}{2}\right)(M_x\hat{E}_{l,m+1}-2M_x\hat{E}_{l,m}+M_x\hat{E}_{l,m-1})\\ &\quad+\frac{1}{s_l}(M_y\hat{E}_{l+1,m}-M_y\hat{E}_{l,m})-\frac{1}{s_{l-1}}(M_y\hat{E}_{l,m}-M_y\hat{E}_{l-1,m}). \end{aligned} \tag{7.12}$$

Let us now look for solutions to (7.12) of the form

$$\hat{E}_{l,m} = \hat{E}_l \mathrm{e}^{-\mathrm{i}k_y mh}. \tag{7.13}$$

Substituting (7.13) in (7.12), and after performing some algebra, we obtain

$$-\frac{\zeta\omega^2 h^2}{6}\left(\frac{s_l + s_{l-1}}{2}\right)(4\hat{E}_l + \hat{E}_{l-1} + \hat{E}_{l+1}) = \frac{1}{s_l}(\hat{E}_{l+1} - \hat{E}_l) - \frac{1}{s_{l-1}}(\hat{E}_l - \hat{E}_{l-1}), \tag{7.14}$$

where the coefficient ζ is defined as

$$\zeta = 1 - \frac{12}{\omega^2 h^2}\left(\frac{\sin^2(k_y h/2)}{1 + 2\cos^2(k_y h/2)}\right). \tag{7.15}$$

Let k_x and k_x^{pml} be the x components of the wave vector in free space and the PML, respectively. Assuming $\hat{E}_l = \mathrm{e}^{-\mathrm{i}k_x hl}$ in free space, substituting in (7.14), with $\sigma = 0$, we obtain the dispersion relation in free space to be

$$\frac{\omega^2 h^2}{12} = \frac{\sin^2(k_x h/2)}{1 + 2\cos^2(k_x h/2)} + \frac{\sin^2(k_y h/2)}{1 + 2\cos^2(k_y h/2)}. \tag{7.16}$$

The dispersion relation for the FDTD scheme [33] is

$$\frac{\omega^2 h^2}{4} = \sin^2(k_x h/2) + \sin^2(k_y h/2). \tag{7.17}$$

Thus, depending on the magnitude and direction of $\mathbf{k}$, the numerically computed wave has an incorrect phase. As a result a plane wave of the form (7.1) will generally move in an incorrect direction at an incorrect speed. However, from (7.16) we can observe that if $k_x h$ and $k_y h$ are small we have

$$\omega^+(k_x, k_y, h) \to \frac{2\sqrt{3}}{h}\sqrt{\frac{(k_x h)^2 + (k_y h)^2}{12}} = \sqrt{k_x^2 + k_y^2} = |\mathbf{k}|, \text{ as } h \to 0 \tag{7.18}$$

where ω^+ denotes the positive solution. Similarly from (7.17) we obtain that $\omega^+ \to |\mathbf{k}|$, as $h \to 0$. This implies that the effects of dispersion can be reduced to any desired level if we choose a fine enough mesh. To derive the (angular) frequency ω for the fully discrete scheme (6.5), we observe that discretization in time corresponds to replacing ωh in (7.16) by $2\dfrac{h}{\Delta t}\sin\left(\dfrac{\omega\Delta t}{2}\right)$. Let us denote the frequency for the fully discrete scheme (6.5) by $\omega_{\Delta t}$. In the working volume, where $\sigma = 0$, we get the dispersion relation to be

$$\left(\frac{h}{\sqrt{3}\Delta t}\right)^2 \sin^2\left(\frac{\omega_{\Delta t}\Delta t}{2}\right) = \frac{\sin^2(k_x h/2)}{1 + 2\cos^2(k_x h/2)} + \frac{\sin^2(k_y h/2)}{1 + 2\cos^2(k_y h/2)}. \tag{7.19}$$

The *Courant number* is $\eta = c\Delta t/h$ ($c = 1$). Solving for $\omega^+_{\Delta t}$ (positive solution) in (7.19) we obtain

$$\omega^+_{\Delta t} = \frac{2}{\Delta t} \sin^{-1}\left(\frac{\eta h \omega^+(k_x, k_y, h)}{2}\right), \tag{7.20}$$

where ω^+ is the (positive) solution to (7.16), i.e.,

$$\omega^+ = \frac{2\sqrt{3}}{h}\sqrt{\frac{\sin^2(k_x h/2)}{1 + 2\cos^2(k_x h/2)} + \frac{\sin^2(k_y h/2)}{1 + 2\cos^2(k_y h/2)}}. \tag{7.21}$$

We note that η must be chosen such that the frequency $\omega^+_{\Delta t}$ is real. This in turn implies that the argument of $\sin^{-1}$ in (7.20) is bounded by 1. We thus need

$$\eta\left(\max_{(k_x h, k_y h)\in[0,\pi]\times[0,\pi]} \left|h\omega^+(k_x, k_y, h)\right|\right) \leq 2 \implies \eta \leq \frac{2}{\sqrt{24}} = \frac{1}{\sqrt{6}} \approx 0.4082, \tag{7.22}$$

In the case of the FDTD scheme a similar analysis yields the stability result

$$\eta \leq \frac{1}{\sqrt{2}} \implies \frac{c\Delta t}{h} \leq \frac{1}{\sqrt{2}} \approx 0.7071, \tag{7.23}$$

with $c = 1$.

Figure 4 compares the dispersion in the FEM scheme and the FDTD scheme for free space, for four different wave propagation angles, $\theta = 0, 15, 30, 45$ degrees, with $\eta = 0.4$. The x axis denotes the number of grid points per wavelength, L/h, where L is the free space wavelength, and the y axis is the numerical phase velocity, v_p, normalized to the speed of light, v_p/c ($c = 1$). We note that, in both the schemes, the phase velocity is the lowest at 45 degrees, implying that the dispersion is the least along the diagonal of the mesh elements; a fact that will be evident in other results to be presented. In Figure 5, similar results are presented for $\eta = 0.01$. We note that the dispersion present in the FEM scheme decreases as the value of η is decreased from 0.4 to 0.01, while the reverse is true in the case of the FDTD scheme. The major effects of dispersion are seen in the case of 10 or less nodes per wavelength. In all cases, as L/h becomes large the convergence of v_p to c ($= 1$) is clearly seen.

The dispersion relation in the PML is obtained in a similar fashion. Let us consider σ to be a constant. Assuming $\hat{E}_l = \mathrm{e}^{-\mathrm{i}k_x^{\mathrm{pml}} hl}$ in the PML, substituting in (7.14), we obtain the dispersion relation in the PML to be

$$\frac{\omega^2 h^2}{12} = \left(\frac{1}{s^2}\right)\frac{\sin^2(k_x^{\mathrm{pml}} h/2)}{1 + 2\cos^2(k_x^{\mathrm{pml}} h/2)} + \frac{\sin^2(k_y h/2)}{1 + 2\cos^2(k_y h/2)}. \tag{7.24}$$

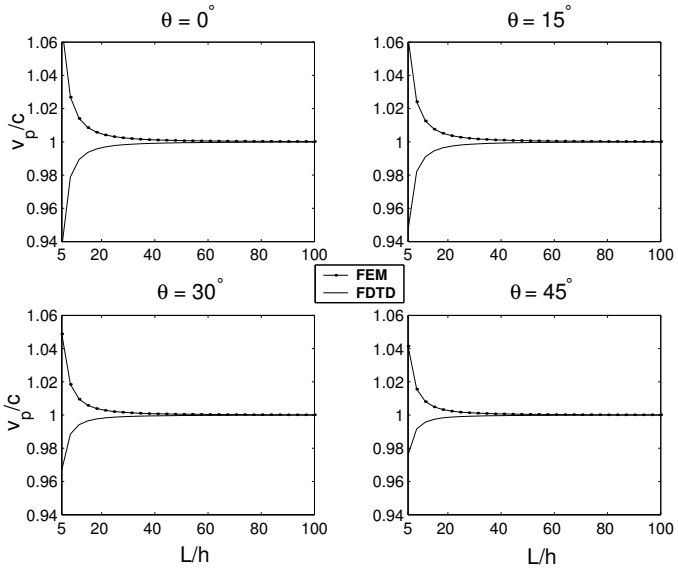

Figure 4: Comparison of the dispersion present in the FEM and the FDTD scheme for selected angles of wave propagation with $\eta = 0.4$.

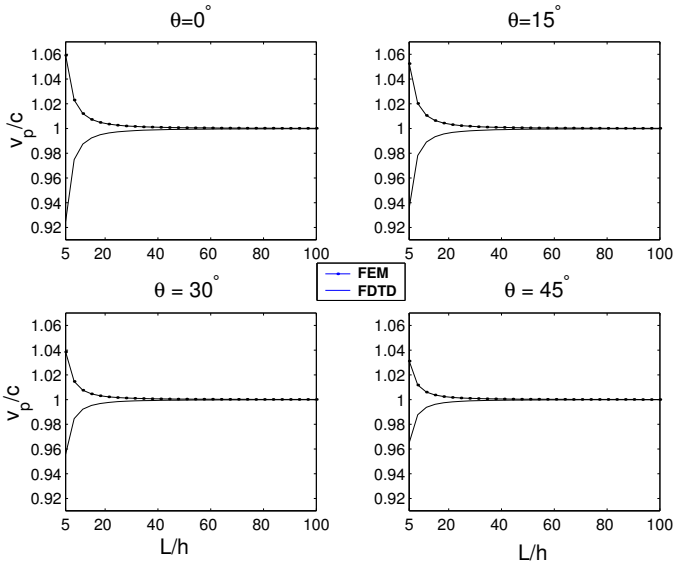

Figure 5: Comparison of the dispersion present in the FEM and the FDTD scheme for selected angles of wave propagation with $\eta = 0.01$.

To derive the dispersion relation for the fully discrete scheme, we again replace ωh by $2\frac{h}{\Delta t}\sin\left(\frac{\omega\Delta t}{2}\right)$ to get

$$\frac{h^2}{3(\Delta t)^2}\sin^2\left(\frac{\omega_{\Delta t}\Delta t}{2}\right) = \left(\frac{1}{s^2}\right)\frac{\sin^2(k_x^{\rm pml}h/2)}{1+2\cos^2(k_x^{\rm pml}h/2)} + \frac{\sin^2(k_y h/2)}{1+2\cos^2(k_y h/2)}. \tag{7.25}$$

7.2 Analysis of the Phase Error and Anisotropy

The phase error that results from the dispersion, expressed in degrees per wavelength, is defined as

$$\delta_p = 360^\circ\left|\frac{\tilde{k}-k}{k}\right|, \tag{7.26}$$

where $\tilde{k}$ is the numerical wave number with which the plane wave propagates in the numerical grid. The wave number for the continuous case is k. Figure 6 is a polar graph of the phase error for selected values of $L/h = 2\pi/kh$ as a function of θ for the FEM and FDTD schemes, with $\eta = 0.4$ (top) and $\eta = 0.01$ (bottom). From Figure 6, we see that, for both the schemes, the smallest error occurs when the plane wave traverses the elements diagonally, whereas the largest error occurs when the wave is propagating along an axis of the mesh Similar observations were made earlier in the plots of v_p/c versus L/h. We note that the phase error in the FEM reduces as the value of η is decreased, whereas, in the FDTD scheme, the phase error increases as the value of η is decreased from 0.4 to 0.01. In Figures 7 and 8, this change in the phase error for the two schemes is more evident. In Figure 7, the phase error is plotted for $\eta = 0.4$ (top) and $\eta = 0.2$ (bottom) and in Figure 8 for $\eta = 0.1$ (top) and $\eta = 0.01$ (bottom). Again, dispersion effects are more evident for the case of 10 nodes per wavelength. As L/h increases the phase error converges to zero, for all angles of propagation. Thus, the effects of dispersion can be reduced to any desired degree by considering a fine enough mesh. Similar results are also obtained for a first order vector finite element method applied to the vector Helmholtz equation [37].

Figure 9 is a log-log graph of the phase error δ_p, versus the number of nodes per wavelength L/h, for selected values of the angle θ, for the FDTD and the FEM schemes. We observe that, for both schemes, as L/h is increased, the error becomes smaller. For large values of L/h the graphs are linear, indicating the error to be proportional to the square of the inverse of the number of nodes per wavelength, i.e., to $(h/L)^2$. This implies the second order convergence, with respect to (h/L), of $\tilde{k}$ to k. We also note that the phase error is lower for

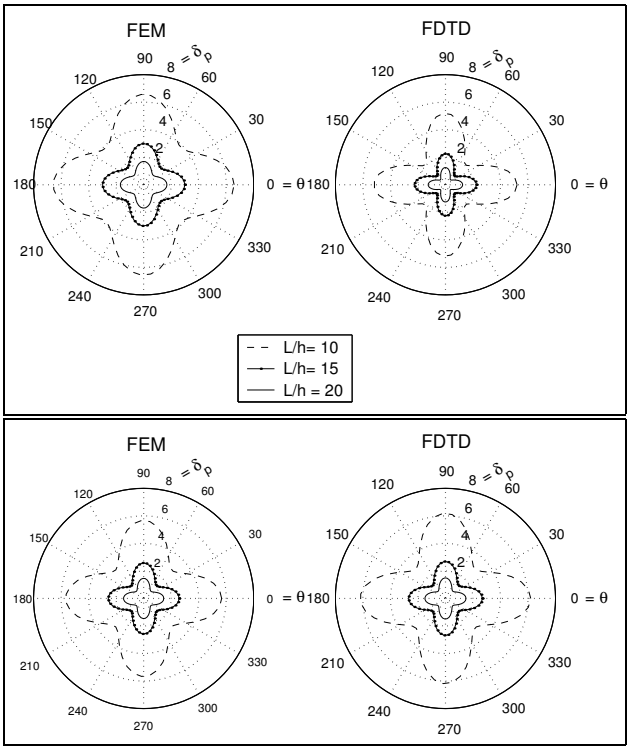

Figure 6: Polar graph of the phase error in degrees per wavelength for selected values of L/h, with $\eta = 0.4$ (top) and $\eta = 0.01$ (bottom).

the FDTD scheme than for the FEM scheme when $\eta = 0.4$, but as η is decreased to 0.01, the effects of dispersion increase for the FDTD scheme.

We present here another important feature of numerical dispersion, which is the anisotropy of the dispersion with respect to the angle of incidence of the propagating wave. In ordinary wave propagation, energy propagates perpendicular to the wave front. When there is anisotropy dispersion, the angle will not be perpendicular. The anisotropy, ϑ, is defined as

$$\vartheta \ = \max_{0\leq\theta\leq\pi/2}\delta_p - \min_{0\leq\theta\leq\pi/2}\delta_p. \tag{7.27}$$

In Tables 1 and 2, we present the maximum and minimum values, over all angles of propagation, of the phase error δ_p, for 10, 15, 20, 30, and 40 nodes per wavelength. We also present the anisotropy present in the FEM and FDTD schemes, for $\eta = 0.4$ and $\eta = 0.01$, respectively. In Table 1, with $\eta = 0.4$, we see that the maximum and the minimum values of δ_p are larger in the case of the FEM scheme; however, the anisotropy is less in the case of the FEM.

In Table 2, with $\eta = 0.01$, we see that the maximum and minimum values of the FDTD

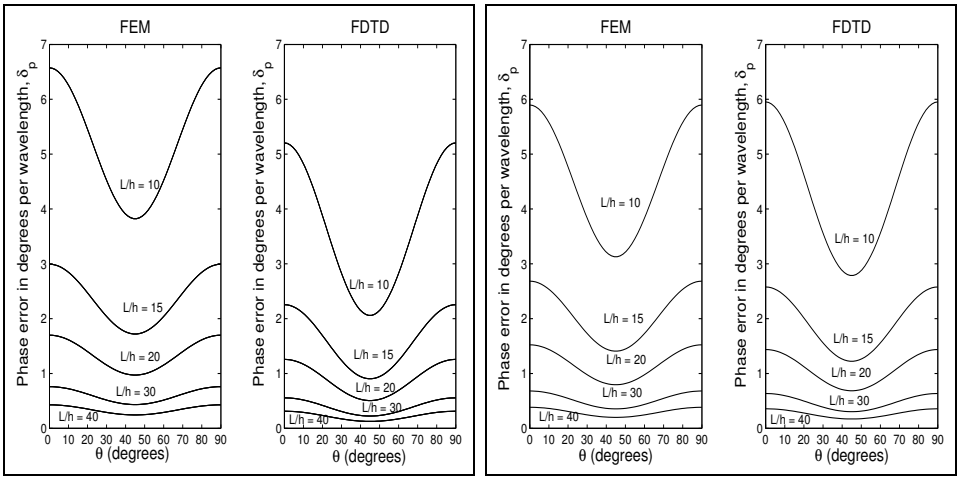

Figure 7: Phase error in degrees per wavelength as a function of the angle θ for selected values of L/h, with $\eta = 0.4$ (left box) and $\eta = 0.2$ (right box).

L/h	FEM			FDTD		
	Max	Min	ϑ	Max	Min	ϑ
10	6.5733	3.8228	2.7505	5.2043	2.0599	3.1444
15	2.9930	1.7204	1.2726	2.2548	0.9044	1.3503
20	1.6981	0.9720	0.7261	1.2573	0.5066	0.7507
30	0.7594	0.4334	0.3260	0.5539	0.2245	0.3309
40	0.4281	0.2441	0.1841	0.3117	0.1261	0.1856

Table 1: Anisotropy for $\eta = 0.4$, for selected values of L/h.

scheme are now larger than the respective values in the FEM scheme. The anisotropy is also smaller for the case of the FEM.

7.3 Calculation of the Reflection Coefficient

In this section we study the properties of the discrete FEM-PML model by performing a plane wave analysis to calculate the reflection coefficient. In the discrete setting the PML model is no longer perfectly matched since the discretization introduces some error which manifests itself as spurious reflections. There is also error that is introduced due to the termination of the PML. We study the errors introduced in the discrete model by calculating the reflection coefficient of an infinite PML (to study the errors caused by the discretization) as well as the reflection coefficient of a finite PML (to study the errors introduced by terminating the PML).

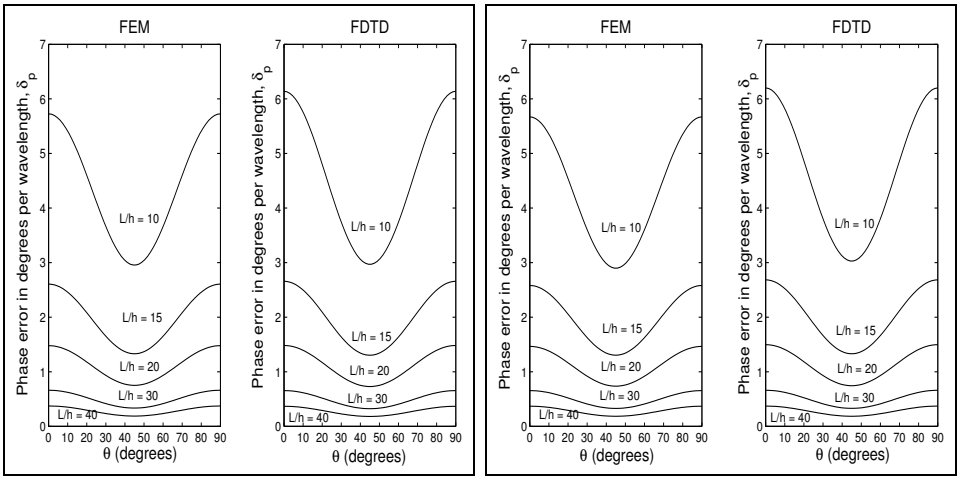

Figure 8: Phase error in degrees per wavelength as a function of the angle θ for selected values of L/h, with $\eta = 0.1$ (left box) and $\eta = 0.01$ (right box).

L/h	FEM			FDTD		
	Max	Min	ϑ	Max	Min	ϑ
10	5.6705	2.8991	2.7714	6.2007	3.0302	3.1705
15	2.5812	1.3043	1.2769	2.6850	1.3298	1.3552
20	1.4643	0.7368	0.7275	1.4970	0.7447	0.7522
30	0.6548	0.3285	0.3263	0.6612	0.3299	0.3312
40	0.3691	0.1850	0.1841	0.3711	0.1854	0.1857

Table 2: Anisotropy for $\eta = 0.01$, for selected values of L/h.

For simplicity we again assume in this section that $\epsilon_0 = \mu_0 = 1$. Let us also assume an infinite PML in the region $x > 0$. Thus, $\sigma_y = 0$ and let $\sigma_x = \sigma$. To calculate the reflection coefficient for the infinite PML, we look for solutions to (7.14) of the form

$$\hat{E}_l = \begin{cases} \mathrm{e}^{-\mathrm{i}k_x hl} + R\mathrm{e}^{\mathrm{i}k_x hl}, & \text{for } l < 0, \\ T\mathrm{e}^{-k_x^{\mathrm{pml}} hl}, & \text{for } l > 0. \end{cases} \tag{7.28}$$

The reflection coefficient is R, and T is the transmission coefficient. Consider the equations associated to the node at the interface $l = 0$ and one node each on either side of the interface

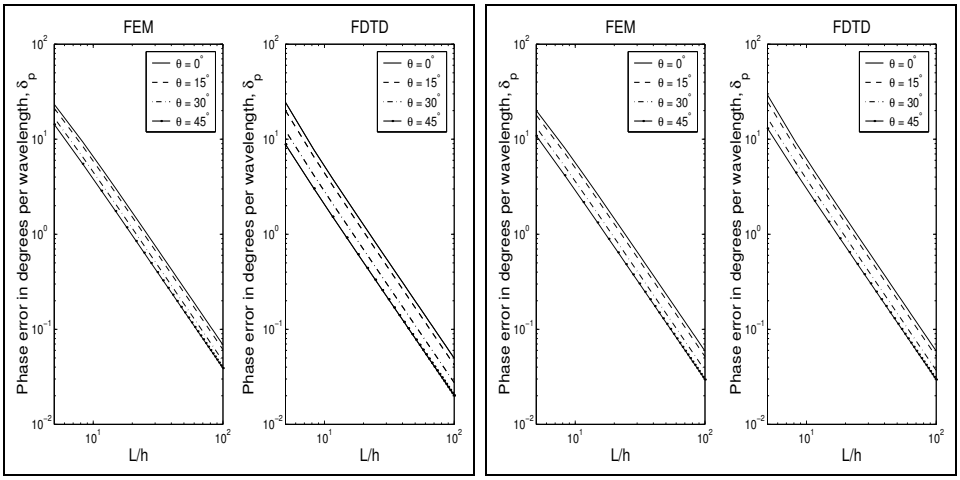

Figure 9: Log-Log plot of the phase error in degrees per wavelength as a function of L/h for selected values of the angle of incidence θ with $\eta = 0.4$ (left box) and $\eta = 0.01$ (right box).

at $l = 1$, and $l = -1$. From (7.14) we have

$$\begin{cases} -\dfrac{\zeta\omega^2h^2}{6}(4\hat{E}_{-1} + \hat{E}_{-2} + \hat{E}_0) = (\hat{E}_0 - \hat{E}_{-1}) - (\hat{E}_{-1} - \hat{E}_{-2}), \\ -\dfrac{\zeta\omega^2h^2}{6}\left(\dfrac{s_0}{2}\right)(4\hat{E}_0 + \hat{E}_{-1} + \hat{E}_1) = \dfrac{1}{s_0}(\hat{E}_1 - \hat{E}_0) - (\hat{E}_0 - \hat{E}_{-1}), \\ -\dfrac{\zeta\omega^2h^2}{6}\left(\dfrac{s_1 + s_0}{2}\right)(4\hat{E}_1 + \hat{E}_0 + \hat{E}_2) = \dfrac{1}{s_1}(\hat{E}_2 - \hat{E}_1) - \dfrac{1}{s_0}(\hat{E}_1 - \hat{E}_0), \end{cases} \tag{7.29}$$

where ζ is defined in (7.15), and s_l is defined in (7.9). Substituting for $\hat{E}_l$ from (7.28) in (7.29) we obtain three equations in the unknowns $\hat{E}_0$, R and T. Solving these resulting equations for R, we can show that the reflection coefficient has the Taylor series expansion

$$R = -\frac{1}{16\omega^2}(\omega^2 - k_y^2)\sigma(\sigma + 2\mathrm{i}\omega)h^2 + \frac{1}{48\omega^3}\sigma^2(\sigma + 2\mathrm{i}\omega)(\omega^2 - k_y^2)^{3/2}h^3 + O(h^4). \tag{7.30}$$

The formula (7.30) implies that the reflection coefficient is proportional to h^2. Thus, the discrete PML model is consistent with the continuous model.

Next, we study the effects of terminating the PML by a PEC. This amounts to setting $\hat{E} = 0$ at the boundary $x = \delta = Mh$ of the PML, i.e. $\hat{E}_M = 0$. To obtain the reflection coefficient we write equation (7.14) for all the nodes in the PML as well as for the node at the interface of the working volume and PML, $\hat{E}_0$, and node $\hat{E}_{-1}$ in the working volume which is h distance away from the interface. Assuming that we know the value of $\hat{E}_{-2}$ we

obtain a system of equations

$$A\mathbf{E} = -(\omega^2 h^2 \zeta + 6) E_{-2} \tilde{e_1}. \tag{7.31}$$

In the above $\mathbf{E} = [\hat{E}_{-1}, \hat{E}_0, \hat{E}_1, \cdots, \hat{E}_{M-1}]^T$, $\tilde{e_1} = [1, 0, 0, \cdots]^T$ and the matrix of coefficients obtained from (7.14) is

$$A = \begin{bmatrix} b_{-1} & c_0 & 0 & \dots & \dots \\ a_{-1} & b_0 & c_1 & 0 & \dots \\ 0 & a_0 & b_1 & c_2 & \dots \\ & & \ddots & \ddots & \ddots \\ & \dots & 0 & a_{M-2} & b_{M-1} \end{bmatrix}, \tag{7.32}$$

where

$$\begin{aligned} a_l &= \left(\omega^2 h^2 \left(\frac{s_{l+1} + s_l}{2} + \frac{6}{s_l} \right) \right), \\ b_l &= \left(4\omega^2 h^2 \left(\frac{s_{l-1} + s_l}{2} \right) - 6 \left(\frac{1}{s_l} + \frac{1}{s_{l-1}} \right) \right), \\ c_l &= \left(\omega^2 h^2 \left(\frac{s_{l-1} + s_{l-2}}{2} + \frac{6}{s_{l-1}} \right) \right). \end{aligned} \tag{7.33}$$

We can solve system (7.32) for the value of R by using (7.28) for $l = -1$ and $l = -2$. In this case the absolute value of the reflection coefficient is calculated to be

$$|R| = \left| \frac{1 + (\omega^2 h^2 \zeta + 6)\kappa \ \mathrm{e}^{\mathrm{i}k_x h}}{1 + (\omega^2 h^2 \zeta + 6)\kappa \mathrm{e}^{-\mathrm{i}k_x h}} \right|, \tag{7.34}$$

where κ is the first diagonal entry in A^{-1}.

Figure 10 plots the reflection coefficient in decibels, Db (i.e., $20 \log_{10} R$), versus the number of nodes per wavelength L/h for different values of R_0, the reflection coefficient at normal incidence. Figure 11 plots the reflection coefficient in Db versus the angle of incidence θ. In these figures we compare the reflection coefficient for the FEM scheme with the reflection coefficient for the TE mode of the Zhao-Cangellaris's PML model using the FDTD scheme which was presented in [14].

We note that the numerical reflection coefficient converges to the reflection coefficient of the continuous model, which is $R_0^{\cos\theta}$ as we increase the value of N. We also note that as θ approaches the value π the numerical reflection coefficient approaches the value 1. This is a well known behavior of PML models, i.e., waves that are propagating transversely to the interface between the domain of interest and a single PML, are not absorbed by the PML. However, these waves get absorbed into the corner regions where two PML's overlap. The

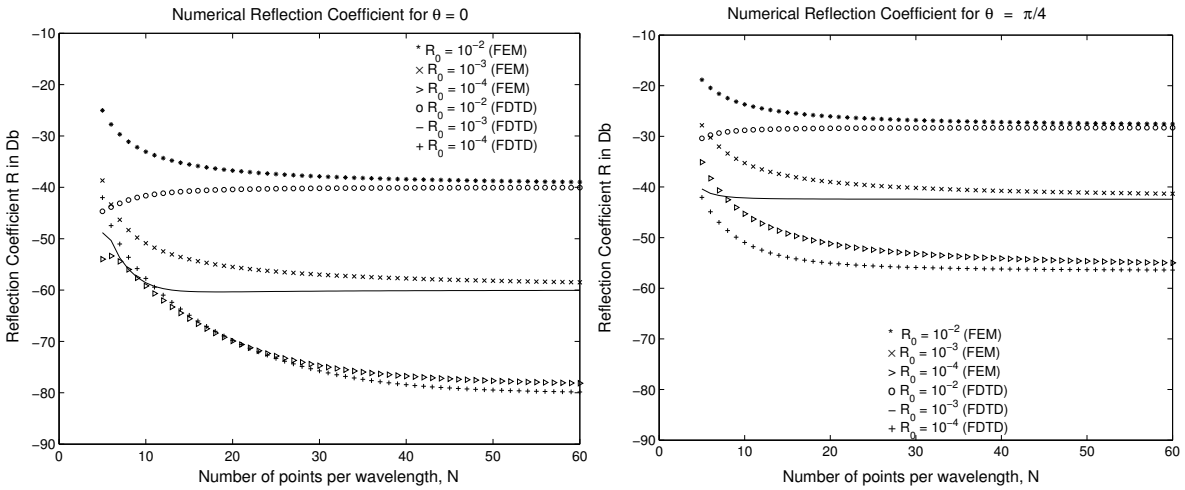

Figure 10: Numerical reflection coefficient for $\theta = 0$ (left) and $\theta = \pi/4$ (right). We note that, as we increase the number of nodes per wavelength, the numerical reflection coefficient in both cases approaches R_0.

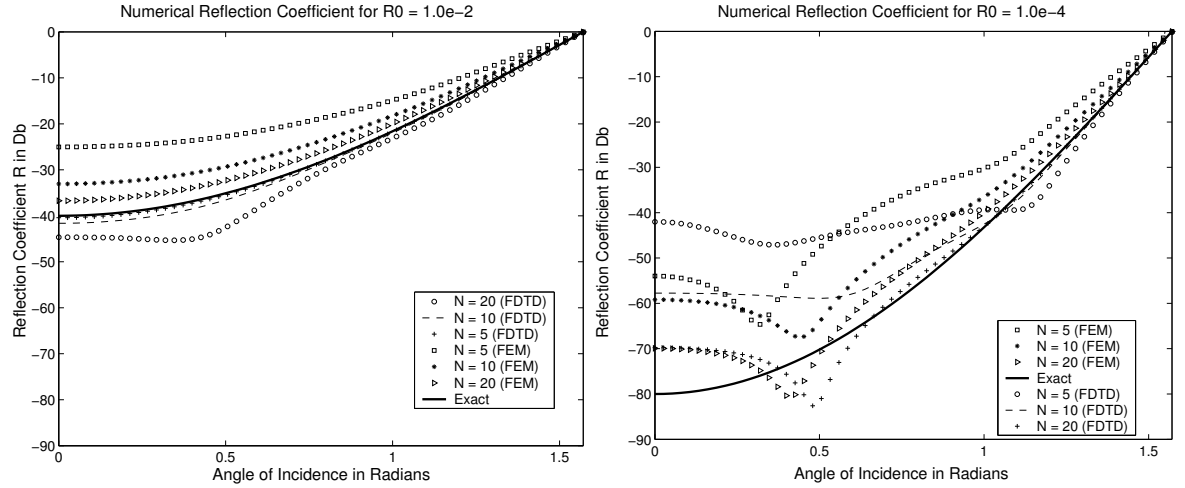

Figure 11: Numerical reflection coefficient for $R_0 = 10^{-2}$ (left), $R_0 = 10^{-4}$ (right). As L/h is increased, the numerical reflection coefficient converges to $R_0^{\cos\theta}$ (Exact).

plots were obtained by considering PML's that are one wavelength thick, i.e., the number of nodes per wavelength is the number of nodes in the PML. The polynomial grading (3.4) was chosen for σ with $m = 2$ and $\sigma_{\max}$ as in (3.5) with $Z = 1$. The PML is in the region $x > 0$. Thus, $x_0 = 0$ in (3.4) for $\alpha = x$.

The power of the polynomial grading for σ has an effect on the numerical reflection errors as is known from analysis of PML models discretized using the FDTD scheme. In Figure 12 (top), we plot the reflection coefficient for the FDTD and FEM schemes against the number of points per wavelength for $m = 2.55$ and $m = 8.65$, with $\theta = 0$ degrees, $R_0 = 10^{-4}$ in each case. In Figure 12 (bottom), we plot the reflection coefficient (FEM) against the number of points per wavelength and m for $\theta = 0$ degrees, $R_0 = 10^{-4}$. Both these figures demonstrate the strong influence of the power m of the polynomial grading for σ on the reflection coefficient.

8 Absorption of a Pulse on the Boundaries of a Computational Domain

The numerical experiment described in this section evaluates the performance of the UPML when a pulse strikes the boundaries of a computational domain. We measure the amount of reflection that an outward propagating pulse produces as it moves from free space to a boundary surrounded by absorbing PML's as in Figure 1.

We choose our domain Ω to be the square $[0, 12] \times [0, 12]$, with a source located at the center $(6, 6)$ of the square. The domain is surrounded by absorbing layers on all four boundaries. We discretize the problem with a rectangular grid composed of 90×90 square elements of step size $h = 2/15$ and the time step is $\Delta t = 0.04/c$, which satisfies the CFL condition (7.22). The source is taken to be the function [12],

$$f(x, y, t) = f_1(x, y) f_2(t),$$

where

$$f_2(t) = \begin{cases} -2\pi^2 f_0^2 (t - t_0) \mathrm{e}^{-\pi^2 f_0^2 (t-t_0)^2}, & \text{if } t \le 2t_0, \\ 0, & \text{if } t \ge 2t_0. \end{cases} \tag{8.1}$$

In the above, $f_0 = \dfrac{c}{20h}$ is the central frequency and $t_0 = 1/f_0$. The function $f_1(x, y)$ is defined as

$$f_1(x, y) = \mathrm{e}^{-7\sqrt{(x-6)^2+(y-6)^2}}. \tag{8.2}$$

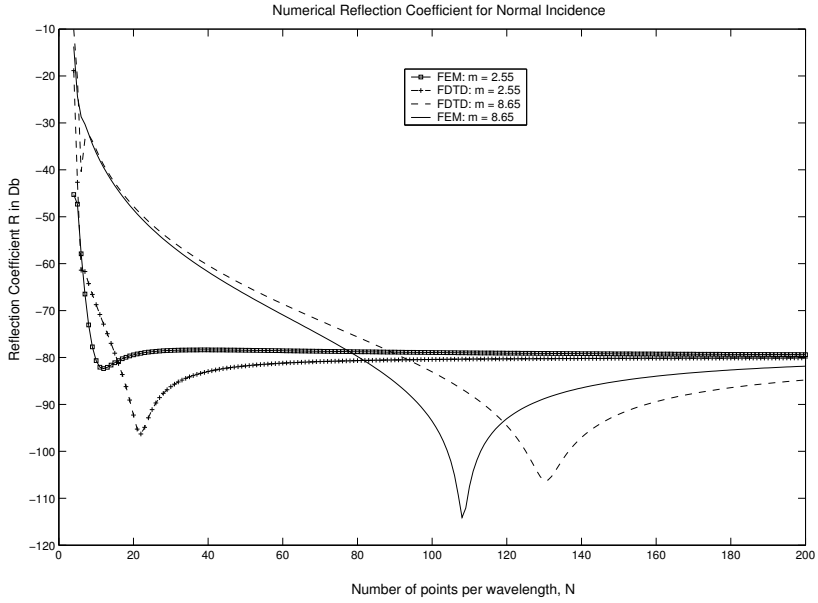

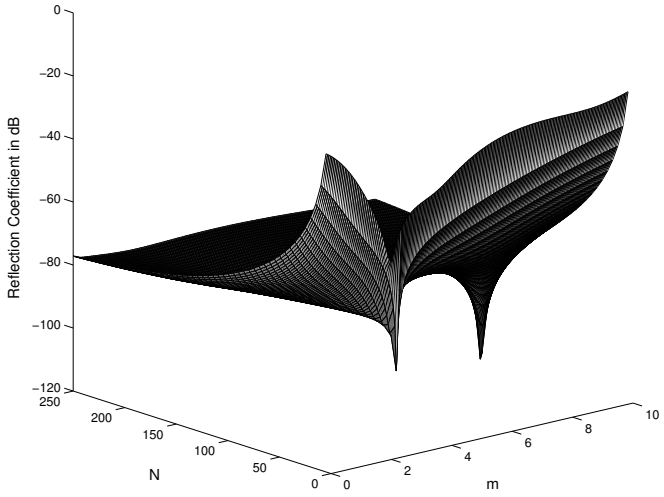

Figure 12: (top) Numerical reflection coefficient for FDTD and FEM in two cases; $m = 2.55$ and $m = 8.65$. (bottom) Numerical reflection coefficient for different points per wavelength and different m values. In both figures $\theta = 0$, $R_0 = 10^{-4}$.

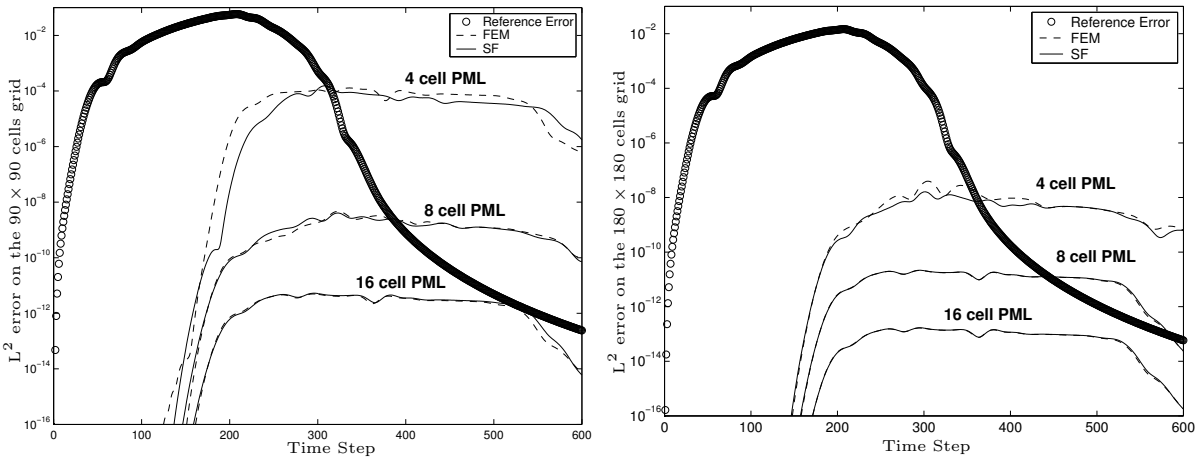

Figure 13: Comparison of the L^2 error for the UPML with a mixed finite element scheme and the split field PML with the FDTD scheme on a 90×90 cells grid (left) and for a 180×180 cells grid (right). We note that as the grid is refined and/or as the number of PML cells is increased the error in the FEM and FDTD schemes is identical.

We obtain a reference solution by using a similar finite element scheme for the TM mode of Maxwell's equations on a larger domain Ω_R containing 360×360 square elements, and the same mesh step size and time step. The domain Ω_R is terminated using PEC conditions on its boundary. We have used the polynomial grading (3.4) for σ with the optimal value of $\sigma_{\max}$ as given in (3.6) with $m = 3.5$.

The L^2 norm of the error due to numerical reflections, which arise due to the finite PML terminated by PEC conditions, is obtained by subtracting at each time step the field E at any grid point inside Ω, from the field E at the corresponding point in Ω_R, taking the square of this difference and summing such differences over all grid points in Ω. We do the above for three PML's containing 4, 8 and 16 cells. A comparison is presented with respect to the split field PML (SF) of Berenger, using the same test problem. The reference solution for the split-field case is constructed in a similar way. Figure 13 shows the L^2 error between the two reference solutions (Reference Error) for the split-field and the finite element schemes, and the L^2 error of the two schemes for 4, 8 and 16 cell PML's each.

From Figure 13 (left), we can see that the reference error (discretization error) dominates for about 250 time steps. After this, as the wave exits the computational domain, the reflection error due to the PEC backed PML takes over. We have used 20 nodes/wavelength (i.e., $L/h = 20$) in our calculations. As can be seen for a 16 cell PML the reflection error is lower than the reference error. Figure 13 (right) shows the L^2 error between the two

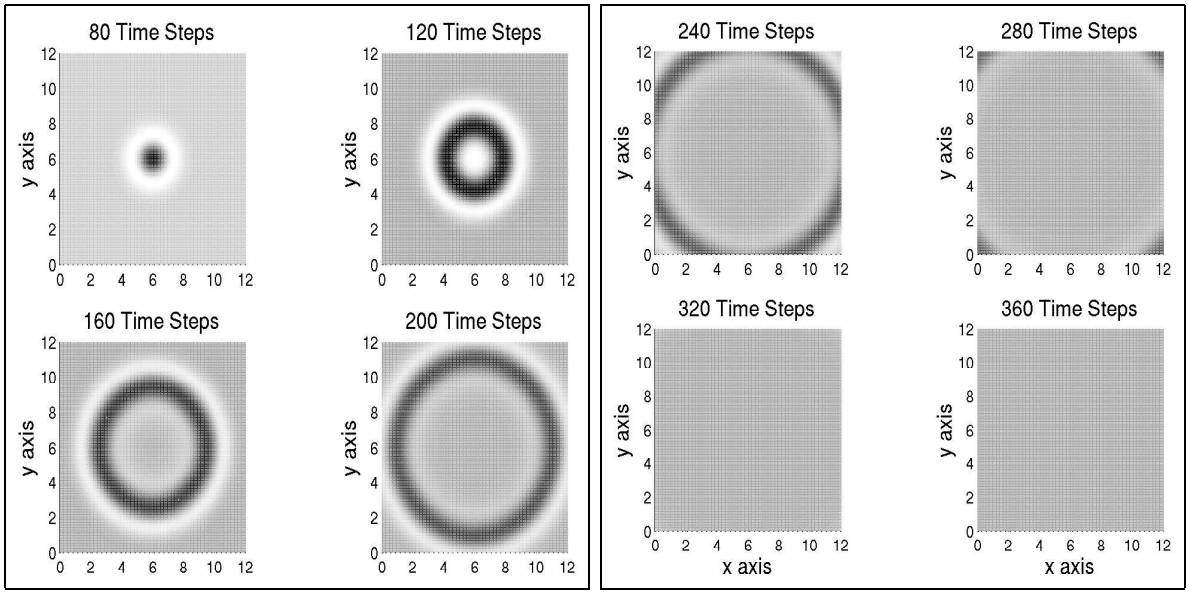

Figure 14: Propagation of the wave front. A top view of the solution is plotted at different time steps. The magnitude of the solution is the same for all time steps.

reference solutions (Reference error) of the split-field and the finite element scheme, and the L^2 error of the two schemes for 4, 8 and 16 cell PML's, for a refined discretization. In this case, $h = 1/15$ and $\Delta t = 0.02/c$. From Figure 13 (right) we can see that a four cell PML provides a good absorbing layer.

In Figure 14, we plot the propagation of a pulse on a 180×180 cells domain backed by an eight cell PML obtained using the FEM scheme. The wave front completely disappears from the domain, as seen in the subplot corresponding to 320 time steps. All subplots are plotted at the same magnitude.

9 Conclusion

In this paper, we have presented and analyzed a mixed finite element scheme for the numerical solution of the 2D TM mode of the uniaxial PML. We have stated energy estimates under certain assumptions. Based on these estimates and the dispersion and reflection coefficient analysis of the scheme we can conclude that the proposed scheme has absorbing properties that are comparable to those of PML models discretized using FDTD. The extension of the mixed FEM to 3D is straightforward and uses a combination of Nédelec's elements and Nédelec-Raviart-Thomas elements for the discretization of the electric and magnetic fields, respectively.

As in the case of the FDTD method, we also find here that the choice of the PML conductivity affects the numerical reflection errors. Thus, a more rigorous analysis is needed to determine the optimal choice of the polynomial approximation to the PML conductivity that will minimize the numerical reflection errors that are generated.

Acknowledgments

The authors would like to thank Dr. H. T. Banks, Dr. R. Glowinski, and Dr. Mac Hyman for fruitful discussions and for their tremendous support and encouragement. This work was supported in part by Los Alamos National Laboratory, an affirmative action/equal opportunity employer which is operated by the University of California for the United States Department of Energy under contract W-7405-ENG-36, in part by the Department of Energy under Contract Nos. 03891-001-99-4G, 74837-001-03 49, and/or 86192-001-04 49 from the Los Alamos National Laboratory, and in part by the U.S. Air Force office of Scientific Research under grants AFOSR F49620-01-1-0026 and AFOSR FA9550-04-1-0220.

References

[1] S. Abarbanel and D. Gottlieb, *A mathematical analysis of the PML method*, J. Comput. Phys., 134 (1997), pp. 357–363.

[2] S. Abarbanel, D. Gottlieb, and J. S. Hesthaven, *Well-posed perfectly matched layers for advective acoustics*, J. Comput. Phys., 154 (1999), pp. 266–283.

[3] A. Ahland, D. Schulz, and E. Voges, *Accurate mesh truncation for Schrödinger equations by a perfectly matched layer absorber: Application to the calculation of optical spectra*, Phys. Rev. B, 60 (1999), pp. 109–112.

[4] E. Bécache and P. Joly, *On the analysis of Berenger's perfectly matched layers for Maxwell's equations*, Math. Model. Numer. Anal., 36 (2002), pp. 87–119.

[5] E. Bécache, P. Joly, and C. Tsogka, *An analysis of new mixed finite elements for the approximation of wave propagation problems*, SIAM J. Numer. Anal., 37 (2000), pp. 1053–1084.

[6] J. P. Berenger, *A perfectly matched layer for the absorption of electromagnetic waves*, J. Comput. Phys., 114 (1994), pp. 185–200.

[7] ——, *Three dimensional perfectly matched layer for the absorption of electromagnetic waves*, J. Comput. Phys., 127 (1996), pp. 363–379.

[8] V. A. Bokil and R. Glowinski, *An operator splitting scheme with a distributed Lagrange multiplier based fictitious domain method for wave propagation problems*, J. Comput. Phys., 205 (2005), pp. 242–268.

[9] ——, *A distributed Lagrange multiplier based fictitious domain method for Maxwell's equations*, Int. J. Comput. Numer. Anal. Appl., (To appear).

[10] L. Brillouin, *Wave Propagation and Group Velocity*, Pure Appl. Phys., Academic Press, New York and London, 1960.

[11] W. C. Chew and W. H. Weedon, *A 3D perfectly matched medium from modified Maxwells equations with stretched coordinates*, Microwave Opt. Technol. Lett., 7 (1994), pp. 599–604.

[12] G. Cohen, P. Joly, J. Roberts, and N. Tordjman, *Higher order triangular finite elements with mass lumping for the wave equation*, SIAM J. Numer. Anal., 38 (2001), pp. 2047–2078.

[13] G. Cohen and P. Monk, *Mur-Nédélec finite element schemes for Maxwell's equations*, Computer Methods in Applied Mechanics and Engineering, 169 (1999), pp. 197–217.

[14] F. Collino and P. Monk, *Optimizing the perfectly matched layer*, Comput. Methods Appl. Mech. Engrg., 164 (1998), pp. 157–171.

[15] R. Dautray and J.-L. Lions, *Mathematical Analysis and Numerical Methods for Science and Technology*, vol. 3, Springer-Verlag, Berlin Heidelberg, 1990.

[16] S. D. Gedney, *An anisotropic perfectly matched layer absorbing media for the truncation of FDTD lattices*, IEEE Trans. Antennas Propagat., 44 (1996), pp. 1630–1639.

[17] M. E. Hayder, F. Q. Hu, and M. Y. Hussaini, *Towards perfectly absorbing conditions for Euler equations*, in AIAA 13th CFD Conference, Paper 97-2075, 1997.

[18] F. Q. Hu, *On absorbing boundary conditions for linearized Euler equations by a perfectly matched layer*, J. Comput. Phys., 129 (1996), pp. 201–219.

[19] D. Johnson, C. Furse, and A. Tripp, *Application and optimization of the perfectly matched layer boundary condition for geophysical simulations*, Microwave Opt. Technol. Lett., 25 (2000), pp. 254–255.

[20] J. S. Juntunen, N. V. Kantartzis, and T. D. Tsiboukis, *Zero reflection coefficient in discretized PML*, IEEE Microwave Wireless Components Lett., 11 (2001), pp. 155–157.

[21] H.-O. Kreiss and J. Lorenz, *Initial Boundary Value Problems and the Navier-Stokes Equations*, vol. 136 of Pure Appl. Math., Academic Press, Boston, USA, San Diego, CA, 1989.

[22] M. Kuzuoglu and R. Mittra, *Investigation of nonplanar perfectly matched abosrbers for finite-element mesh truncation*, IEEE Trans. Antennas Propagat., 45 (1997), pp. 474–486.

[23] J.-F. Lee, R. Lee, and A. Cangellaris, *Time-domain finite element methods*, IEEE Trans. Antennas Propagat., 45 (1997), pp. 430–442.

[24] Y. Liu, *Fourier analysis of numerical algorithms for the Maxwell's equations*, J. Comput. Phys., 124 (1996), pp. 396–416.

[25] R. Mittra and U. Pekel, *A finite element method frequency domain application of the perfectly matched layer (PML) concept*, Microwave Opt. Technol. Lett., 9 (1995), pp. 117–122.

[26] ——, *A new look at the perfectly matched layer (PML) concept for the reflectionless absorption of electromagnetic waves*, IEEE Microwave Guided Wave Lett., 5 (1995), pp. 84–86.

[27] P. Monk, *A comparison of three mixed methods for the time-dependent Maxwell's equations*, SIAM J. Sci. Stat. Comput., 13 (1992), pp. 1097–1122.

[28] P. G. Petropoulos, *An analytical study of the discrete perfectly matched layer for the time-domain maxwell's equations in cylindrical coordinates*, IEEE Trans. Antennas Propagat., 51 (2003), pp. 1671–1675.

[29] P. G. Petropoulos, L. Zhao, and A. C. Cangellaris, *A reflectionless sponge layer absorbing boundary condition for the solution of Maxwell's equations with higher order staggered finite difference schemes*, J. Comput. Phys., 139 (1998), pp. 184–208.

[30] C. M. Rappaport, *Perfectly matched absorbing boundary conditions based on anisotropic lossy mapping of space*, IEEE Microwave Guided Wave Lett., 5 (1995), pp. 90–92.

[31] P. A. Raviart and J. M. Thomas, *A mixed finite element method for 2nd order elliptic problems*, in Proc. of Math. Aspects on the Finite Element Method, I. Galligani and E. Magenes, eds., vol. 606 of Lecture Notes in Mathematics, Springer-Verlag, 1977, pp. 292–315.

[32] Z. S. Sacks, D. M. Kinsland, R. Lee, and J. F. Lee, *A perfectly matched anisotropic absorber for use as an absorbing boundary condition*, IEEE Trans. Antennas Propagat., 43 (1995), pp. 1460–1463.

[33] A. Taflove, *Advances in Computational Electrodynamics: The Finite-Difference Time-Domain method*, Artech House, Norwood, MA, 1998.

[34] J. Tang, K. Paulsen, and S. Haider, *Perfectly matched layer mesh truncations for nodal-based finite-element methods in electromagnetic scattering*, IEEE Trans. Antennas Propagat., 46 (1998), pp. 507–516.

[35] L. N. Trefethen, *Group velocity in finite difference schemes*, SIAM Rev., 24 (1982), pp. 113–136.

[36] R. Vichnevetsky and J. Bowles, *Fourier Analysis of Numerical Approximations of Hyperbolic Equations*, SIAM Studies in Applied Mathematics, SIAM, 1982.

[37] G. S. Warren and W. R. Scott, *An investigation of numerical dispersion in the vector finite element method using quadrilateral elements*, IEEE Trans. Antennas Propagat., 42 (1994), pp. 1502–1508.

[38] J. We, D. Kinsland, J. Lee, and R. Lee, *A comparison of anistropic PML to Berenger's PML and it's application to the finite-element method of EM scattering*, IEEE Trans. Antennas Propagat., 45 (1997), pp. 40–50.

[39] J.-Y. Wu, J. Nehrbass, and R. Lee, *A comparison of PML for TVFEM and FDTD*, Int. J. Numer. Model., 13 (2000), pp. 233–244.

[40] Z. Wu and J. Fang, *High performance PML algorithms*, IEEE Microwave Guided Wave Lett., 6 (1996), pp. 335–337.

[41] K. S. Yee, *Numerical solution of initial boundary value problems involving Maxwell's equations in isotropic media*, IEEE Trans. Antennas Propagat., 14 (1966), pp. 302–307.

[42] L. Zhao and A. Cangellaris, *A general approach for the development of unsplit-field time-domain implementations of perfectly matched layers for FDTD grid truncation*, IEEE Microwave Guided Wave Lett., 6 (1996), pp. 209–211.